Molecular Motion of Spin Labeled Side Chains in α-Helices: Analysis by Variation of Side Chain Structure†

Linda Columbus,‡,⊥ Támás Kálai,§,⊥ József Jekö,|| Kálmán Hideg,§ and Wayne L. Hubbell*,‡

Jules Stein Eye Institute and Department of Chemistry and Biochemistry, University of California, Los Angeles, California 90095-7008, Institute of Organic and Medicinal Chemistry, University of Pécs H-7643 Pécs, P. O. Box 99, Hungary, and ICN Alkaloida Co. Ltd., H-4440, Tiszavasvári, P. O. Box 1, Hungary

Received November 16, 2000; Revised Manuscript Received January 25, 2001

ABSTRACT: Two single cysteine substitution mutants at helix surface sites in T4 lysozyme (D72C and V131C) have been modified with a series of nitroxide methanethiosulfonate reagents to investigate the structural and dynamical origins of their electron paramagnetic resonance spectra. The novel reagents include 4-substituted derivatives of either the pyrroline or pyrrolidine series of nitroxides. The spectral line shapes were analyzed as a function of side chain structure and temperature using a simulation method with a single order parameter and diffusion rates about three orthogonal axes as parameters. Taken together, the results provide strong support for an anisotropic motional model of the side chain, which was previously proposed from qualitative features of the spectra and crystal structures of spin labeled T4 lysozyme. Site-specific differences in apparent order parameter are interpreted in terms of backbone dynamics modes with characteristic correlation times in the nanosecond or faster time scale. The saturated 4-substituted pyrrolidine nitroxides are shown to be a suitable template for novel "functionalized" side chains designed to mimic salient features of the native side chains they replace.

Site-directed spin labeling (SDSL)[1] has emerged as a useful approach for the investigation of protein structure and dynamics (*1*−*3*). SDSL utilizes site-directed mutagenesis to replace the residue of interest with a cysteine and all reactive native cysteine residues with a suitable substitute. The unique cysteine residue is then modified with a sulfhydryl-specific nitroxide reagent to introduce a paramagnetic side chain sensitive to the local environment. In most previous studies, the side chain designated here as R1(a) has been employed (Figure 1), although other side chains have been introduced for specific purposes (*4*, *5*).

The EPR spectrum of a spin labeled side chain in a protein encodes information on the dynamic modes of the nitroxide. Such information is of interest because the nitroxide motion reflects a variety of structural and dynamic features of the protein itself. These include Brownian rotary diffusion, backbone dynamics, and bond rotational isomerizations within the side chain, the latter being modulated by interactions of the side chain with its environment. In principle,

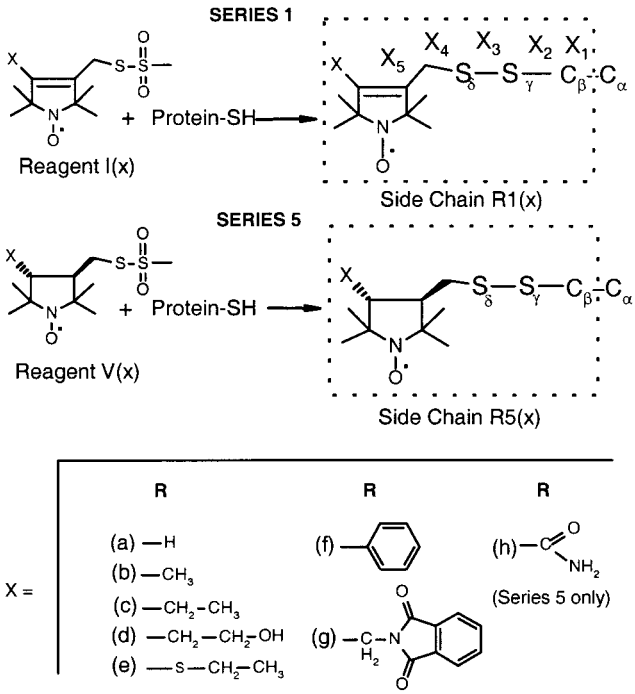

FIGURE 1: Reactions of spin labeling reagents I(x) and V(x) with a protein sulfhydryl group to generate the corresponding side chains R1(x) and R5(x). The various 4-substituents (x) are designated (a−h), as indicated. For the R1(x) side chain, the dihedral angles associated with each bond are defined as X_1−X_5.

† Research reported here was supported by NIH Grants EYO5216, T3 EY07026, and T32 GM08496 (W.L.H.), the Jules Stein Professor Endowment (W.L.H.), Bruce Ford Bundy and Anne Smith Bundy Foundation (W.L.H.), Grants Hungarian National Research Foundation (OTKA T030013) (K.H.), and Hungarian Ministry of Education (FKFP 0252/1999) (K.H.).

* To whom correspondence should be addressed. Wayne L. Hubbell: UCLA-JSEI, 100 Stein Plaza BH-973, Los Angeles, CA 90095-7008, phone: (310) 206-8830, fax: (310) 794-2144, e-mail: hubbellw@jsei.ucla.edu.

‡ University of California.

§ University of Pécs.

|| ICN Alkaloida Co. Ltd.

⊥ These authors contributed equally.

[1] Abbreviations: SDSL, site-directed spin labeling; EPR, electron paramagnetic resonance; T4L, T4 lysozyme; IPTG, isopropyl-β-thiogalactoside; PCR, polymerase chain reaction; MOPS, 3-(*N*-morpholino) propane-sulfonic acid; EDTA, disodium ethylenediamine tetraacetate; SDS−PAGE, sodium dodecyl sulfate−polyacrylamide gel electrophoresis; MOMD, microscopic order macroscopic disorder, RMS, root-mean-square; *S*, order parameter; NMR, nuclear magnetic resonance.

10.1021/bi002645h CCC: $20.00
Published on Web 03/10/2001

one can deduce the dynamic modes of the nitroxide from spectral simulations and deconvolute the contributions from each of these features. The rate and amplitude of backbone fluctuations and the internal dynamics of the side chain are of particular interest and are the subjects of the present communication.

For membrane-bound proteins and globular proteins with molecular mass ≥ 50 kD, Brownian rotational diffusion is too slow to contribute to spectral averaging for conventional X-band (9.5 GHz) EPR. For smaller globular proteins, such as T4L (molecular mass ≈ 17 kD), effects of Brownian diffusion can be reduced by working in solutions of increased viscosity (*4*−*6*) or with the use of high-frequency EPR (*6*). Thus, it is generally possible in EPR spectroscopy to study the effects of backbone fluctuations and internal side chain motions without interference from rotary diffusion.

Some progress has been made in analyzing internal side chain motion in terms of protein structure. For this purpose, the inverse central linewidth (δ^{-1}) and the second moment ($\langle H^2 \rangle$) of the R1(a) EPR spectrum have been used as measures of nitroxide "mobility" that reflect both rate and amplitude of motion (*4*). With these measures, correlations between the mobility of R1(a) and protein topography have been established in the helical proteins T4 lysozyme (T4L) (*4*), colicin E1 (*7*), annexin XII (*8*), and the T domain of diphtheria toxin (*9*). In all of these proteins, R1(a) residues are highly immobilized at buried sites, are immobilized or have complex multicomponent spectra at tertiary contact sites, and have intermediate mobility at helix surface sites. These distinctions arise from differences in side chain interactions with the environment. The simple relationship between side chain mobility and protein topography is sufficient to determine sequence-specific secondary structure using the periodic modulation of mobility with sequence position (*2*, *4*).

While the above studies provided a general relationship between nitroxide mobility and protein topography, they also revealed mobility effects that could not be accounted for by differences in topographical location. For example, at X-band frequency, the EPR spectra for R1(a) at different solvent-exposed helix surface sites reflect similar degrees of mobility that clearly distinguish them from buried and tertiary contact sites (*4*). Nevertheless, the mobility of R1(a) at each of these sites is unique in quantitative detail and is a "fingerprint" for the sequence position of the residue (*4*, *5*). For R1(a) at the majority of helix surface sites investigated so far, the sequence-specific mobility differences are apparently not determined by differences in interaction with the nearest neighbors in the same helix (*4*). This was dramatically illustrated in T4L with a "transmutation" experiment where the nearest neighbors around R1(a) at one helix surface site were mutated to the same as those around R1(a) at a topologically similar site in a different helix. The unique EPR spectra and mobility of R1(a) at each site were retained (*4*).

The most attractive proposal to account for the site-specific mobility is that backbone dynamic modes with correlation times in the nanosecond regime modulate the side chain internal motions. If this were the case, SDSL may be a powerful new tool for mapping backbone dynamics in proteins, particularly for high molecular weight soluble proteins and membrane proteins. To identify putative backbone contributions to R1(a) mobility, and establish a quantitative scale for their measurement, it is necessary to have a model for the internal modes of motion of the R1(a) side chain in the absence of rotary diffusion, backbone fluctuations, or side chain interactions. With this foundation in place, the effect of the other contributions can be included experimentally, one at a time.

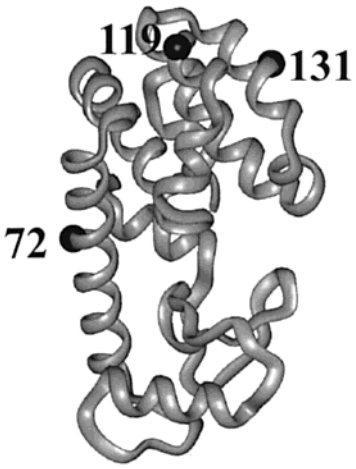

FIGURE 2: Ribbon structure of T4 lysozyme (pdb ID: 3lzm) with spheres indicating the location of the solvent-exposed helical sites: 72, 119, and 131.

The internal dynamic modes of R1(a) on a solvent-exposed site in a α-helix without tertiary interactions are determined by the internal bond rotations. Recently, a crystallographic analysis has provided structural models of the R1(a) side chain at solvent-exposed helical sites in T4L (*10*). In the structures, the disulfide group is relatively fixed in position, thus fixing the average values of the dihedral angles X_1 and X_2 (see Figure 1 for the definition of the dihedral angles). The g^+g^+ ($X_1 \approx 300$, $X_2 \approx 300$) conformation may be the energy minimum in the absence of local or tertiary interactions (*10*). The disulfide bond has $X_3 \approx \pm 90$ (g^+, g^-). Interconversion between the states has a free energy of activation of ≈ 6.6−9 kcal/mol (*11*) and, thus, is too slow to contribute to the nitroxide motions observed experimentally (see below). Collectively, the above features suggest a model for the side chain internal motion that involves torsional oscillations of X_4 and X_5 of the R1(a) side chain as dominant contributors to the motion of the nitroxide. This will be referred to hereafter as the X_4/X_5 model for internal motion.

A primary goal of the present work is to quantitatively evaluate the X_4/X_5 model of the R1(a) side chain using T4L as a model system. To investigate the internal motion of the side chain in isolation, it is necessary to select a site for placement of R1(a) that has minimal backbone flexibility and at the same time one at which R1(a) makes no tertiary contact interactions and has no interactions with nearest neighbors in the same helix. Solvent-exposed site 72, in the center of the long interdomain helix of T4L (Figure 2), appears to be an ideal candidate and was selected as a reference for initial study. The mobility of 72R1(a) is essentially independent of nearest neighbor side chains, and no tertiary contacts are made (*4*). Additionally, site 72 is one of the most highly ordered helix surface sites in the protein, with low Debye−Waller factors in the crystal structure (*12*) and slow amide hydrogen exchange (*13*), indicating a relatively rigid backbone structure. Thus, we

tentatively assume that the motion of 72R1(a) is dominated by internal bond rotations of the side chain. One outcome of the present studies is to provide additional support for this assumption.

To investigate putative contributions of backbone motions to side chain mobility, site 131 in T4L was selected for comparison with site 72. Site 131 is located in a short two-turn helix (Figure 2), and like 72R1(a), the mobility of 131R1(a) does not appear to depend on nearest neighbor interactions (*4*). However, on the basis of the Debye−Waller factors for 131 in the crystal structure (*12*) and the high hydrogen exchange rate as compared to 72 (*13*), 131R1(a) is predicted to have additional dynamical modes from backbone flexibility. Quantitative comparison of the motion of 72 and 131 may thus provide insight into the contribution from backbone dynamics.

The experimental strategy to evaluate the X_4/X_5 model for R1(a) is to selectively perturb the motion of the side chain by chemical modification of the nitroxide ring, and compare the results, judged by spectral simulation, with that predicted by the model. Side chains based on both the pyrrole nitroxides of series 1 and the pyrrolidine nitroxides of series 5 with 4-substituents of increasing size and varying degrees of polarity (Figure 1) were investigated at both 72 and 131.

The results for the reference site 72 suggest a simple anisotropic motion in R1(a) that strongly supports the X_4/X_5 model. Importantly, the spectrum of 131R1(a) can be simulated with the same type of anisotropic motion as 72R1(a) but with a simple increase in the amplitude of the motion. Moreover, the spectra of R1(a) at helix surface sites in other proteins can also be accounted for by the same anisotropic motion with a variable amplitude and possibly rate of motion. These results are consistent with a model in which backbone fluctuations in the nanosecond regime modulate an anisotropic motion described by the X_4/X_5 model. Although a rigorous description of R1 motion in terms of rates and amplitudes of each dynamic mode must await future multifrequency and single-crystal EPR analysis, the results presented here provide a firm foundation for the design of experiments to further evaluate the model.

At some helix surface sites, multicomponent spectra are observed, indicating multiple dynamic states of R1. Even some single-component spectra, such as that for 131R1(a) at room temperature, become multicomponent at reduced temperature. The additional components are believed to arise from weak local interactions, and temperature is proposed as a useful variable to "titrate" these weak interactions.

The series 1 and 5 derivatives were designed to analyze the internal motions of the R1(a) side chain, but they may be useful spin labels in their own right. For example, 4-substituted derivatives of series 1 have hindered rotations about the two terminal bonds due to steric interactions of the substituent with the S_δ sulfur atom. Thus, the residual motion in these derivatives should have an enhanced contribution from backbone modes, and they may find use as specific probes of backbone motion. The 4-phenyl and 4-phthalimido derivatives [R1(f) and R1(g), respectively], which have additional interactions with the protein, are sufficiently hindered to be effectively immobilized at both surface sites studied. This property will make them useful as probes for measurement of overall protein rotational diffusion.

Scheme 1[a]

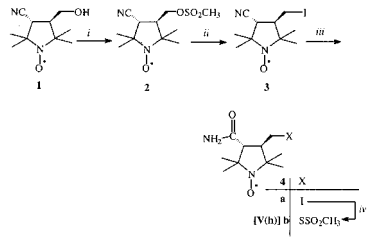

[a] *i*: MsCl, Et_3N, CH_2Cl_2, 0 °C → r.t., 1 h, 82%; *ii*: NaI, acetone, 55 °C, 10 h, 72%; *iii:* 30% H_2O_2, MeOH, H_2O, cat. K_2CO_3, r.t. 3 h, 72%; i*v*: $NaSSO_2CH_3$, DMSO, 30 min, 70 °C, 41%.

Unlike the case for series 1, some 4-substituted derivatives of series 5 retain high mobility. Thus, 4-substituents of this series may be used to design a new class of functionalized nitroxide side chains in which the mobility is sufficiently high to allow detection of changes in mobility due to interactions of the substituent.

EXPERIMENTAL PROCEDURES

Materials. Spin labeling reagents **I(a)** (*14*), **I(g)** (*15*), **I(e)** (*16*), **I(h)** (*17*), and compounds **1** (*18*), **9a** (*19*), **9b** (*19*), **17** (*20*), **23** (*21*), **28** (*18*), **30** (*22*), **33** (*23*) were prepared according to published procedures. Flash column chromatography was performed on silica gel with a Merck Kieselgel 60 (0.040−0.063 mm) and qualitative TLC was carried out on commercially prepared plates coated with Merck Kieselgel GF_{254}. Resource S and Hi-Trap desalting columns were purchased from Amersham-Phamacia Biotech (Piscataway, NJ). The cysteine-free pseudo-wild-type lysozyme gene containing the substitutions C54T and C97A was kindly provided by F. W. Dahlquist (University of Oregon). This will be referred to as "wild type" or T4 lysozyme. Taq Polymerase and restriction enzymes were purchased from Fisher (Tustin, CA). IPTG was purchased from Alexis Biochemicals (San Diego, CA) and Tris, MOPS, and EDTA were purchased from Fisher (Tustin, CA). Microcon centrifugal filter devices for protein concentration were purchased from Millipore (Bedford, MA). Capillaries for EPR measurements were purchased from VitroCom Inc. (Mountain Lakes, NJ).

Synthesis of Spin Labeling Reagents.

General. Melting points were determined on a Boetius micro melting point apparatus and are uncorrected. Elemental analyses (C, H, N, and S) were performed on EA 1110 CHNS Elemental analyzer, or the halogens were analyzed titrimetrically by Schöniger's method. IR spectra were recorded on Zeiss Specord 75, and 1H NMR spectra of corresponding diamagnetic compounds were recorded with a Varian-Gemini 200 spectrometer using $CDCl_3$ as a solvent and TMS as an internal standard. Mass spectra were recorded on a VG TRIO-2 instrument.

*Synthesis of V(h) (**4b**, Scheme 1). (a) 1-Oxyl-trans-3-(methylsulfonyloxymethyl)-4-cyano-2,2,5,5-tetramethylpyrrolidine (**2**).* To a stirred solution of compound **1** (1.97 g, 10.0 mmol) and Et_3N (1.11 g, 11.0 mmol) in CH_2Cl_2 (30 mL) methanesulfonyl chloride (1.25 g, 11.0 mmol) was added dropwise at 0 °C. The mixture was stirred at r.t. for 1 h. The organic phase was washed with brine (10 mL), separated,

dried ($MgSO_4$), filtered, and evaporated to yield **2** as a crystalline solid 2.25 g (82%), mp 149−150 °C. IR (Nujol) ν_{max} 2230 cm^{-1}. Anal: calcd. for $C_{11}H_{19}N_2O_4S$ (275.34), C: 47.98, H: 6.96, N: 10.17, S: 11.64; found C: 47.81, H: 7.00, N: 10.11, S: 11.52. MS *m*/*z*, (%): 275 (M^+, 16), 261 (10), 245 (4), 68 (100).

*(b) 1-Oxyl-trans-3-iodomethyl-4-cyano-2,2,5,5-tetramethylpyrrolidine (**3**).* A solution of compound **2** (1.38 g, 5.0 mmol) and NaI (1.50 g, 10.0 mmol) in dry acetone (30 mL) was stirred and refluxed for 10 h. After acetone was evaporated off, the residue was dissolved in EtOAc (30 mL) and washed with brine (15 mL). The organic phase was dried, filtered, evaporated, and purified with flash column chromatography (hexane/Et_2O) to give compound **3** as a crystalline solid 1.10 g (72%), mp 134−135 °C. IR (Nujol) ν_{max} 2235 cm^{-1}. Anal: calcd. for $C_{10}H_{16}IN_2O$ (307.15), C: 39.10, H: 5.25, N: 9.12; found C: 39.20, H: 5.27, N: 9.05. MS *m*/*z*, (%): 307 (M^+, 17), 293 (6), 277 (3), 69 (100).

*(c) 1-Oxyl-trans-3-iodomethyl-4-carboxamido-2,2,5,5-tetramethylpyrrolidine (**4a**).* To a solution of **3** (1.53 g, 5.0 mmol) in MeOH (10 mL), aq. 30% H_2O_2 solution (5 mL) and K_2CO_3 (69 mg, 0.5 mmol) were added, and the mixture was allowed to stand at r.t. for 3 h. The mixture was extracted with $CHCl_3$ (2 × 20 mL), and the organic phase was separated, dried ($MgSO_4$), filtered, evaporated, and purified by chromatography (hexane/EtOAc) to give compound **4a** as a crystalline solid 1.17 g (72%), mp 163−164 °C. IR (Nujol) ν_{max} 3470 cm^{-1}, 3360 cm^{-1}, 1660 cm^{-1}, 1625 cm^{-1}. Anal: calcd. for $C_{10}H_{18}IN_2O_2$ (325.16), C: 36.94, H: 5.58, N: 8.62; found C: 36.81, H: 5.57, N: 8.60. MS *m*/*z*, (%): 325 (M^+, 23), 311 (8), 295 (8), 41 (100).

*(d) 1-Oxyl-trans-3-methanesulfonylthiomethyl-4-carboxamido-2,2,5,5-tetramethyl-pyrrolidine (**4b**, reagent V(h)).* A solution of compound **4a** (975 mg, 3.0 mmol) and $NaSSO_2CH_3$ (805 mg, 6.0 mmol) in DMSO (10 mL) was cautiously heated to 70 °C, and the mixture was monitored by TLC. After consumption of starting material (30 min), the solution was poured onto water (30 mL). The aq. solution was extracted with $CHCl_3$ (2 × 30 mL), the organic phase was separated, dried ($MgSO_4$), filtered, evaporated, and the residue was purified by flash chromatography (hexane/EtOAc) to yield the title compound **4b** as a dark-brown oil 380 mg (41%). IR (neat) ν_{max} 3460 cm^{-1}, 3360 cm^{-1}, 2960 cm^{-1}, 2920 cm^{-1}, 1660 cm^{-1}, 1630 cm^{-1}. Anal: calcd. for $C_{11}H_{21}N_2O_4S_2$ (309.42), C: 42.70, H: 6.84, N: 9.05, S: 20.72; found C: 42.63, H: 6.87, N: 9.09, S: 20.59. MS *m*/*z*, (%): 309 (M^+, 1), 295 (1), 279 (2), 41 (100).

*Synthesis of I(d) (**9b**, Scheme 2). (a) 1-Oxyl-3-ethyl-4-methylen-2,2,5,5-tetramethylpyrrolidine (**5c**).* To a solution of compound **5b** (2.61 g, 10.0 mmol) in THF (20 mL), SMEAH (5 mL, 70% in toluene) was added dropwise at 0 °C, and the mixture was stirred at r.t. for 4 h. The reaction mixture was cautiously poured onto a mixture of crushed ice (70 g) and 10% NaOH solution (30 mL). The aqueous solution was extracted with THF (2 × 30 mL). The organic phase was separated, dried ($MgSO_4$), filtered, and evaporated. Purification with flash column chromatography (hexane/Et_2O) yielded compound **5c** as an orange oil 940 mg (52%). IR (neat) ν_{max} 2965 cm^{-1}, 2920 cm^{-1}, 1660 cm^{-1}. Anal: calcd. for $C_{11}H_{20}NO$ (182.29), C: 72.48, H: 11.06, N: 7.69; found C: 72.38, H: 11.10 N: 7.65. MS *m*/*z*, (%): 182 (M^+, 60), 152 (88), 135 (35), 42 (100).

Scheme 2[a]

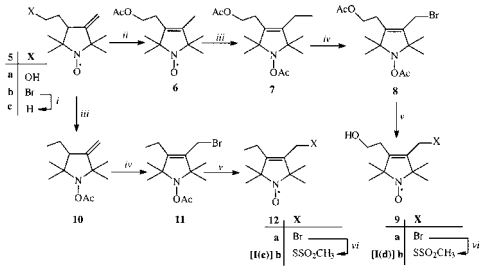

[a] *i*: SMEAH, THF, 0 °C → r.t., 4 h, 52%; *ii*: 5a, AcCl, Et_3N, CH_2Cl_2, 0 °C → r.t., 1 h, 78%; *iii*: (1) ascorbic acid, dioxane, H_2O, 40 °C, 15 min. (2) AcCl, Et_3N, $CHCl_3$, 0 °C → r.t., 1 h, 50−66%; i*v*: NBS, benzoyl peroxide, CCl_4, 76 °C, 30 h, 55−57%; *v*: (1) $NaOCH_3$, THF, r.t., 20 min, (2) MnO_2, $CHCl_3$, O_2, r.t., 20 min, 20−40%; *vi*: EtOH, H_2O, $NaSSO_2CH_3$, 78 °C, 20 min, 35−42%.

*(b) 1-Oxyl-3-acetoxyethyl-4-methylen-2,2,5,5-tetramethylpyrrolidine (**6**).* Acetyl chloride (1.25 g, 16.0 mmol) was added dropwise to a stirred solution of compound **5a** (2.97 g, 15.0 mmol) and Et_3N (1.62 g, 16.0 mmol) in CH_2Cl_2 (30 mL) at 0 °C. The mixture was stirred at r.t. for 1 h. The mixture was washed with brine (15 mL), and the organic phase was separated, dried ($MgSO_4$), filtered, and evaporated. Then, the residue was purified with flash chromatography (hexane/Et_2O) to give **6** as an orange oil 2.80 g (78%). IR (neat) ν_{max} 2970 cm^{-1}, 2920 cm^{-1}, 1730 cm^{-1}, 1660 cm^{-1}. Anal: calcd. for $C_{13}H_{22}NO_3$ (240.32), C: 64.97, H: 9.23, N: 5.83; found C: 65.01, H: 9.25 N: 5.78. MS *m*/*z*, (%): 240 (M^+, 23), 226 (18), 107 (71), 43 (100).

*(c) 1-Acetoxy-3-acetoxyethyl-4-methylen-2,2,5,5-tetramethylpyrrolidine (**7**).* To a solution of radical **6** (2.40 g, 10.0 mmol) in dioxane (30 mL), a solution of ascorbic acid (7.04 g, 40.0 mmol) in water (25 mL) was added. The mixture was stirred at 40 °C for 15 min under N_2. The colorless solution was extracted with $CHCl_3$ (2 × 20 mL) and dried $MgSO_4$ under N_2. First, Et_3N (1.11 g, 11.0 mmol) was added and, then, acetyl chloride (863 mg, 11.0 mmol) at 0 °C. The mixture was stirred at r.t. for 1 h. The mixture was filtered and evaporated to dryness. The residue was taken up in brine (20 mL), extracted with EtOAc (2 × 20 mL), dried ($MgSO_4$), filtered, and evaporated. The residue was purified by flash chromatography (hexane/Et_2O) to yield compound **7** as a colorless oil 1.41 g (50%). ^1H NMR (200 MHz, $CDCl_3$) δ 4.95 (dd, 2H, J = 2 Hz, J = 2 Hz), 4.35−4.02 (m, 2H), 2.48 (t, 1H, J = 6.3 Hz), 2.13 (s, 3H), 2.06 (s, 3H), 1.88−1.72 (m, 2H), 1.28 (s, 3H), 1.25 (s, 3H), 1.16 (s, 3H), 0.96 (s, 3H). IR (neat)ν_{max} 2960 cm^{-1}, 2930 cm^{-1}, 1760 cm^{-1}, 1730 cm^{-1}, 1650 cm^{-1}. Anal: calcd. for $C_{15}H_{25}NO_4$ (283.37), C: 63.58, H: 8.89, N: 4.97; found C: 63.59, H: 9.05; N: 4.91. MS *m*/*z*, (%): 283 (M^+, 2), 268 (18), 241 (31), 226 (100).

*(d) 1-Acetoxy-3-acetoxyethyl-4-bromomethyl-2,5-dihydro-2,2,5,5-tetramethyl-1H-pyrrole (**8**).* A mixture of diacetate **7** (1.20 g, 4.2 mmol), *N*-bromosuccinimide (900 mg, 5.0 mmol) and benzoyl peroxide (24 mg, 0.1 mmol) in CCl_4 (30 mL) was refluxed for 30 h. The succinimide was filtered off and washed with CCl_4 (10 mL). The filtrate was evaporated to dryness, dissolved in EtOAc (30 mL), and washed with brine (10 mL). The organic phase was separated, dried ($MgSO_4$), filtered, and evaporated in vacuo. The residue was purified by flash chromatography with (hexane/Et_2O) to give compound **8** as a yellow oil 836 mg (55%). ^1H NMR

(200 MHz, $CDCl_3$) δ 4.18 (t, 3H, $J = 6.3$ Hz), 4.06−3.93 (m, 2H), 2.6−2.4 (m, 2H), 2.15 (s, 3H), 2.05 (s, 3H), 1.31 (s, 6H), 1.21 (s, 6H). IR (neat) ν_{max} 2965 cm^{-1}, 2925 cm^{-1}, 1750 cm^{-1}, 1740 cm^{-1}, 1650 cm^{-1}. Anal: calcd. for $C_{15}H_{24}BrNO_4$ (362.26), C: 49.73, H: 6.68, Br: 22.06 N: 3.87; found C: 49.28, H: 6.60, Br: 21.95, N: 3.91. MS *m/z*, (%): 361 (M^+, 1), 346 (19), 304 (67), 43 (100).

(e) 1-Oxyl-3-hydroxyethyl-4-bromomethyl-2,5-dihydro-2,2,5,5-tetramethyl-1H-pyrrole ***(9a)***. A solution of **8** (800 mg, 2.2 mmol) in THF (20 mL) was treated with 0.2 M NaOMe solution (2 mL) in MeOH. The mixture was allowed to stand at r.t. and was monitored by TLC. After consumption of the starting material (20 min), the organic solvents were evaporated off. The residue was dissolved in saturated aqueous NH_4Cl solution and extracted with $CHCl_3$ (2 × 30 mL). The organic phase was separated, dried ($MgSO_4$), filtered, and evaporated. The residue was dissolved in $CHCl_3$ (20 mL), activated MnO_2 (86 mg, 1.0 mmol) was added, and O_2 was bubbled through the solution for 20 min. The solution was filtered, the organic solvent was evaporated off, and the residue was purified by chromatography (hexane/EtOAc) to give **9a** as a pale yellow crystalline solid 243 mg (40%), mp 69−71 °C. IR (Nujol) ν_{max} 3360 cm^{-1}, 1640 cm^{-1}. Anal: calcd. for $C_{11}H_{19}BrNO_2$ (277.18), C: 47.67, H: 6.91, Br: 28.83, N: 5.05; found C: 47.58, H: 6.90, Br: 28.71, N: 5.08. MS *m/z*, (%): 276 (M^+, 16), 262 (10), 196 (14), 182 (100).

(f) 1-Oxyl-3-hydroxyethyl-4-methanesulfonylthiomethyl-2,5-dihydro-2,2,5,5-tetramethyl-1H-pyrrole ***(9b****, reagent I(d))*. Compound **9a** (200 mg, 0.73 mmol) and $NaSSO_2CH_3$ (134 mg, 1.0 mmol) were refluxed in EtOH (10 mL) and water (5 mL) for 20 min. The EtOH was evaporated off. Brine (10 mL) was added, and the residue was extracted with $CHCl_3$ (2 × 15 mL). The organic phase was separated, dried ($MgSO_4$), filtered, and evaporated. Purification of the residue with flash column chromatography on silica gel ($CHCl_3$/Et_2O) gave **9b** as an off-white solid 79 mg (35%), mp 77−79 °C. IR (Nujol) ν_{max} 3360 cm^{-1}, 1640 cm^{-1}. Anal: calcd. for $C_{12}H_{22}NO_4S_2$ (308.43), C: 46.73, H: 7.19, N: 4.54, S: 20.79; found C: 46.68, H: 6.98 N: 4.58, S: 20.95. MS *m/z*, (%): 308 (M^+, 5), 292 (10), 277 (10), 43 (100).

Synthesis of I(c) ***(12b****, Scheme 2). (a) 1-Acetoxy-3-ethyl-4-methylen-2,2,5,5-tetramethylpyrrolidine* ***(10)***. Compound **5c** (910 mg, 5.0 mmol) was converted to protected derivative **10** with ascorbic acid (3.52 g, 20.0 mmol) followed by treatment with acetyl chloride (471 mg, 6.0 mmol) in the presence of Et_3N (606 mg, 6.0 mmol) under the same reaction conditions and procedures as in the case of compound **7**. Purification by chromatography (hexane/Et_2O) yielded **10** as a colorless oil 742 mg (66%). ^1H NMR (200 MHz, $CDCl_3$) δ 4.9 (d, 2H, $J = 2$ Hz), 2.1 (s, 3H), 2.1−0.95 (m, 6H), 1.28 (s, 3H), 1.21 (s, 3 H), 1.15 (s, 3H), 0.95 (s, 3H); IR (neat) ν_{max} 2965 cm^{-1}, 2925 cm^{-1}, 1770 cm^{-1}, 1650 cm^{-1}. Anal: calcd. for $C_{13}H_{23}NO_2$ (225.53), C: 69.30, H: 10.29, N: 6.22; found C: 69.15, H: 10.25 N: 6.30.

(b) 1-Acetoxy-3-ethyl-4-bromomethyl-2,5-dihydro-2,2,5,5-tetramethyl-1H-pyrrole ***(11)***. The above protected derivative **10** (676 mg, 3.0 mmol), *N*-bromosuccinimide (534 mg, 3.0 mmol) and benzoyl peroxide (24 mg, 0.1 mmol) were refluxed in CCl_4 (30 mL) for 30 h and worked up under the same reaction conditions as in the case of compound **8.** Purification by chromatography (hexane/Et_2O) gave compound **11** as a yellow oil 519 mg (57%). ^1H NMR (200 MHz, $CDCl_3$) δ 4.0 (s, 2H), 2.15 (s, 3H), 1.75−0.95 (m, 5H), 1.30 (s, 6H), 1.20 (s, 6H); IR (neat) ν_{max} 2960 cm^{-1}, 2920 cm^{-1}, 1765 cm^{-1}, 1645 cm^{-1}. Anal: calcd. for $C_{13}H_{22}BrNO_2$ (304.23), C: 51.32, H: 7.29, Br: 26.26 N: 4.60; found C: 51.38, H: 7.25 Br: 26.10, N: 4.49. MS *m/z*, (%): 303 (M^+, 2), 288 (22), 246 (100), 182 (56).

(c) 1-Oxyl-3-ethyl-4-bromomethyl-2,5-dihydro-2,2,5,5-tetramethyl-1H-pyrrole ***(12a)***. A solution of **11** (456 mg, 1.5 mmol) in THF (20 mL) was deprotected with 0.2 M NaOMe solution (2 mL) under the same reaction conditions and procedures as in case of compound **9.** Purification with flash column chromatography (hexane/Et_2O) yielded **12a** as yellow crystalline solid 78 mg (20%), mp 60−62 °C. IR (Nujol) ν_{max} 1640 cm^{-1}. Anal: calcd. for $C_{11}H_{19}BrNO$ (261.18), C: 50.59, H: 7.33, Br: 30.59 N: 5.36; found C: 50.51, H: 7.35, Br: 30.71, N: 4.33. MS *m/z*, (%): 260 (M^+, 31), 246 (10), 166 (95), 152 (100).

(d) 1-Oxyl-3-ethyl-4-methanesulfonylthiomethyl-2,5-dihydro-2,2,5,5-tetramethyl-1H-pyrrole ***(12b****, reagent I(c))*. A mixture of **12a** (52 mg, 0.2 mmol), $NaSSO_2CH_3$ (67 mg, 0.5 mmol) in EtOH (6 mL) and water (3 mL) was refluxed for 20 min and worked up under the same reaction conditions as in case of compound **9b**. Purification with flash column chromatography (hexane/EtOAc) yielded **12b** as a yellow oil 24 mg (42%). IR (Nujol) ν_{max} 2970 cm^{-1}, 2920 cm^{-1}, 1640 cm^{-1}. Anal: calcd. for $C_{12}H_{22}NO_3S_2$ (292.43), C: 49.29, H: 7.58, N: 4.76, S: 21.93; found C: 49.33, H: 7.62, N: 4.73, S: 22.00. MS *m/z*, (%): 292 ($M^{+\bullet}$, 18), 198 (22), 166 (64), 83 (51), 67(42), 55(53), 41(100).

Synthesis of I (b) ***(18b****, Scheme 3). (a) 1-Oxyl-3-methyl-4-methylen-2,2,5,5-tetramethyl-pyrrolidine* ***(15)*** *and 1-Methoxy-3-methyl-4-methylen-2,2,5,5-tetramethyl-pyrrolidine* ***(14)***. Under N_2 atmosphere at −30 °C, a catalytic amount of CuCN (500 mg, 5.5 mmol) was added to a stirred solution of methylmagnesium iodide, which was freshly prepared from methyl iodide (8.46 g, 60.0 mmol) and Mg turnings (1.46 g, 60.0 mmol) in anhydr. Et_2O (80 mL). After 30 min, a solution of allyl ester **13** (7.63 g, 30.0 mmol) in anhydr. THF (20 mL) was added gradually over 20 min. The mixture was stirred at 0 °C for 4 h and then quenched with aq. NH_4Cl solution (30 mL). The organic phase was washed with Et_2O (2 × 50 mL). The combined organic phases were dried ($MgSO_4$), filtered, and evaporated in vacuo to give a pale yellow oil. The residue was taken up in $CHCl_3$ (40 mL), a catalytic amount of activated MnO_2 (86 mg, 1.0 mmol) was added, and O_2 was bubbled through the mixture for 20 min. The deep orange solution was filtered, evaporated again to dryness, and flash chromatographed on silica gel (hexane/Et_2O) as an eluent. The first colorless band was the diamagnetic byproduct **14** as a colorless oil 1.64 g (30%), IR (neat) ν_{max} 2950 cm^{-1}, 2920 cm^{-1}, 1595 cm^{-1}. Anal. calcd. for $C_{11}H_{21}NO$ (183.29), C: 72.08, H: 11.55, N: 7.64; found C: 72.03, H: 11.53, N: 7.70. The second yellow band was compound **15** 1.76 g (35%) as an orange oil. IR (neat) ν_{max} 2970, 2920. Anal: calcd. for $C_{10}H_{18}NO$ (168.27), C: 71.39, H: 10.78, N: 8.32, found C: 71.23, H: 10.80, N: 8.38. MS *m/z*, (%): 168 (M^+, 7), 152(24), 138 (8), 57 (100).

(b) 1-Acetoxy-3-methyl-4-methylen-2,2,5,5-tetramethyl-pyrrolidine ***(16)***. Compound **15** (1.68 g, 10.0 mmol) was reduced with ascorbic acid (7.04 g, 40.0 mmol) and converted to an *N*-acetoxy derivative with acetyl chloride (785 mg, 10.0

Scheme 3[a]

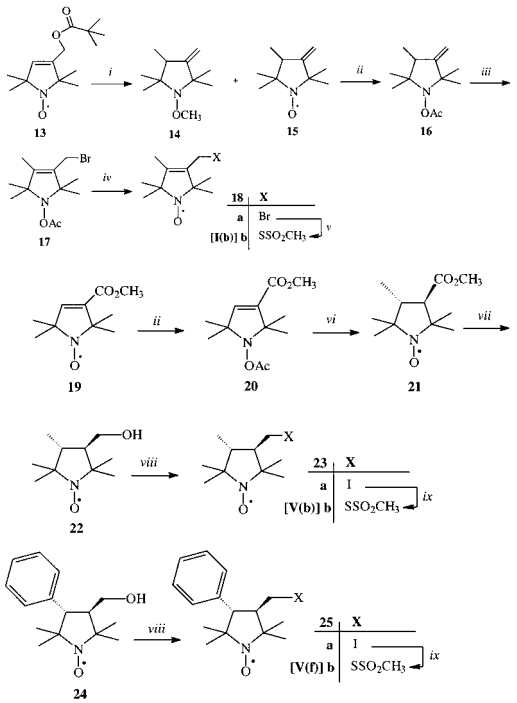

[a] *i:* (1) CH_3MgI, CuCN, Et_2O, −30 °C → 0 °C, 4 h; (2) NH_4Cl, MnO_2, $CHCl_3$, O_2, r.t., 20 min; **14** 30%, **15** 35%; *ii*: (1) ascorbic acid, dioxane, H_2O, 40 °C, 15 min; (2) AcCl, Et_3N, $CHCl_3$, 0 °C → r.t., 1 h, 48−57%; *iii*: NBS, benzoyl peroxide, CCl_4, 76 °C, 30 h, 57%; *iv*: (1) $NaOCH_3$, THF, r.t., 30 min, (2) MnO_2, $CHCl_3$, O_2, r.t., 20 min, 28%; *v*: EtOH, H_2O, $NaSSO_2CH_3$, 78 °C, 20 min, 38%; *vi*: (1) CuI, MeMgI, Et_2O, −30 °C → r.t. 3.5 h, (2) NH_4Cl, MnO_2, $CHCl_3$, O_2, r.t., 20 min; (3) chromatography, NaOMe, THF, r.t., then aq. 5% H_2SO_4, 30%; *vii:* MeOH, *t*-BuOH, $NaBH_4$, 82 °C, 3 h, 53%; *viii*: (1) MsCl, Et_3N, $CHCl_3$, 0 °C → r.t., 1 h; (2) NaI, acetone, 55 °C, 10 h, 41−60%; *ix:* $NaSSO_2CH_3$, DMSO, 60 °C, 30 min, 31−40%.

mmol) in the presence of Et_3N (1.01 g, 10.0 mmol) under the same reaction conditions and procedures as in the case of compound **7**. Purification with chromatography (hexane/Et_2O) gave compound **16** 1.20 g (57%) as a colorless oil. IR (neat) ν_{max} 2960 cm^{-1}, 2920 cm^{-1}, 1765 cm^{-1}, 1655 cm^{-1}. Anal: calcd. for $C_{12}H_{21}NO_2$ (211.30), C: 68.21, H: 10.02, N: 6.63; found C: 68.33, H: 10.05, N: 6.73. MS *m*/*z*, (%): 211 (M^+, 10), 196 (7), 169 (10), 154 (100).

*(c) 1-Acetoxy-3-bromomethyl-4-methyl-2,5-dihydro-2,2,5,5-tetramethyl-1H-pyrrole (**17**).* The above protected derivative **16** (1.05 g, 5.0 mmol) was brominated with *N*-bromosuccinimide (900 mg, 5.0 mmol) in the presence of benzoyl peroxide (24 mg, 0.1 mmol) in CCl_4 (30 mL) under the same reaction procedures and conditions as in the case of compound **8**. Purification with flash column chromatography (hexane/Et_2O) yielded compound **17** as a pale yellow oil 826 mg (57%). ^1H NMR (200 MHz, $CDCl_3$) δ 3.96 (d, 2H, J = 2 Hz), 2.14 (s, 3H), 1.68 (s, 3H), 1.30 (s, 6H), 1.17 (s, 6H). IR (neat) ν_{max} 2960 cm^{-1}, 2920 cm^{-1}, 1760 cm^{-1}, 1660 cm^{-1}. Anal: calcd. for $C_{12}H_{20}BrNO_2$ (290.20), C: 49.67, H: 6.95, Br: 27.53, N: 4.83; found C: 49.70, H: 7.00, N: 4.74. MS *m*/*z*, (%): 289 (M^+, 1), 274 (17), 247 (10), 232 (100).

*(d) 1-Oxyl-3-bromomethyl-4-methyl-2,5-dihydro-2,2,5,5-tetramethyl-1H-pyrrole (**18a**).* A solution of **17** (783 mg, 2.7 mmol) in THF (20 mL) was deprotected with 0.2 M NaOMe (1.5 mL) solution under the same reaction conditions and procedures as in the case of compound **9a**. Purification with flash column chromatography (hexane/Et_2O) gave compound **18a** as an orange solid 186 mg (28%), mp 57−58 °C. IR (Nujol) ν_{max} 2970 cm^{-1}, 2920 cm^{-1}, 1660 cm^{-1}. Anal: calcd. for $C_{10}H_{17}BrNO$ (247.16), C: 48.60, H: 6.93, Br: 32.33 N: 5.67 found C: 48.50, H: 7.00, Br: 32.18, N: 5.76. MS *m*/*z*, (%): 246 (M^+, 9), 231 (5), 167 (10), 152 (100).

*(e) 1-Oxyl-3-methanesulfonylthiomethyl-4-methyl-2,5-dihydro-2,2,5,5-tetramethyl-1H-pyrrole (**18b**, reagent I(b)).* A mixture of compound **18a** (123 mg, 0.5 mmol), $NaSSO_2CH_3$ (134 mg, 1.0 mmol) in EtOH (6 mL) and water 3 (mL) was refluxed for 30 min. The reaction was worked up under the same procedures as in the case of compound **9b**. Purification with flash column chromatography (hexane/EtOAc) gave compound **18b** as an off-white solid 53 mg (38%), mp 62−64 °C. IR (Nujol) ν_{max} 2960 cm^{-1}, 2920 cm^{-1}, 1655 cm^{-1}. Anal: calcd. for $C_{11}H_{20}NO_3S_2$ (278.40), C: 47.46, H: 7.24, N: 5.03, S: 23.03; found C: 47.35, H: 7.18, N: 4.93, S: 23.00. MS *m*/*z*, (%): 278 (M^+, 2), 263 (1), 121 (67), 43 (100).

*Synthesis of V(b) (**23b**, Scheme 3). (a) 1-Acetoxy-3-carboxymethyl-2,5-dihydro-2,2,5,5-tetramethyl-1H-pyrrole (**20**).* Compound **19** (7.92 g, 40.0 mmol) was reduced with ascorbic acid (21.12 g, 0.12 mol) and converted to a protected derivative with acetyl chloride (3.92 g, 50.0 mmol) in the presence of Et_3N (5.05 g, 50.0 mmol) under the same reaction procedures and conditions as in the case of compound **7.** After crystallization of the crude product from hexane, we obtained compound **20** as white crystals 4.62 g, (48%), mp 41−43 °C. ^1H NMR (200 MHz, $CDCl_3$) δ 6.58 (s, 1H), 3.75 (s, 3H), 2.14 (s, 3H), 1.42 (s, 6H), 1.29 (s, 6H). IR (Nujol) ν_{max} 1760 cm^{-1}, 1720 cm^{-1}, 1630 cm^{-1}. Anal: calcd. for $C_{12}H_{19}NO_4$ (241.29), C: 59.73, H: 7.94, N: 5.80; found C: 59.82, H: 7.92, N: 5.76. MS *m*/*z*, (%): 241 (M^+, 2), 226 (6), 199 (15), 184 (100).

*(b) 1-Oxyl-trans-3-methoxycarbonyl-4-methyl-2,2,5,5-tetramethylpyrrolidine (**21**).* Under N_2 atmosphere at −30 °C, a suspension of CuI (7.61 g, 40.0 mmol) was added to a stirred solution of methylmagnesium iodide, which was freshly prepared from methyl iodide (17.03 g, 0.12 mol) and magnesium turnings (2.88 g, 0.12 mol) in anhyd. Et_2O (60 mL). After 30 min, a solution of the unsaturated protected ester **20** (4.50 g, 18.6 mmol) was added in dry Et_2O (50 mL) gradually over 30 min. The mixture was stirred at −30 °C for 3 h. After warming to room temperature, the mixture was poured onto an ice-cooled NH_4Cl solution (50 mL). The organic phase was separated, and the aqueous phase was washed with Et_2O (2 × 30 mL) and $CHCl_3$ (1 × 50 mL). The extracts were combined, dried ($MgSO_4$), filtered, and evaporated. The residue was dissolved in $CHCl_3$ (40 mL), activated MnO_2 (86 mg, 1.0 mmol) was added, and O_2 was bubbled through the solution for 20 min. The MnO_2 was removed by filtration, and the deep orange solution was evaporated to dryness. The product was purified with flash chromatography on silica gel (hexane/Et_2O). The first two yellow bands were the trans and cis isomers of **21**, as yellow oils. The solution of cis and trans isomers in THF (30 mL) was treated with 0.2 M NaOMe solution (1.0 mL). The solvents were evaporated off, and the residue was taken up in 5% aq. H_2SO_4 solution (5 mL), extracted with $CHCl_3$ (30 mL), dried ($MgSO_4$), filtered, and evaporated to give the pure trans isomer **21** as an orange oil 1.19 g (30%). IR (neat) ν_{max} 2960 cm^{-1}, 2920 cm^{-1}, 1730 cm^{-1}. Anal: calcd. for

$C_{11}H_{20}NO_3$ (214.28), C: 61.66, H: 9.41, N: 6.54, found C: 61.62, H: 9.40, N: 6.56. MS *m*/*z*, (%): 214 (M^+, 21), 199 (16), 115 (46), 70 (100).

*(c) 1-Oxyl-trans-3-hydroxymethyl-4-methyl-2,2,5,5-tetramethylpyrrolidine (**22**).* To a stirred solution of ester **21** (1.07 g, 5.0 mmol) and $NaBH_4$ (1.48 g, 40.0 mmol) in anhydr. *t*-BuOH (15 mL), a mixture of anhydr. MeOH (4 mL) and *t*-BuOH (6 mL) was added dropwise over 3 h under N_2. The mixture was concentrated in vacuo, quenched with saturated aqueous NH_4Cl solution (20 mL), extracted with $CHCl_3$ (2 × 20 mL), dried ($MgSO_4$), filtered, and evaporated. The crude alcohol was purified by flash chromatography (hexane/EtOAc) to afford **22** as a yellow oil 492 mg (53%). IR (neat) ν_{max} 3960 cm^{-1}, 2970 cm^{-1}, 2920 cm^{-1}. Anal: calcd. for $C_{10}H_{20}NO_2$ (186.27), C: 64.48, H: 10.82, N: 7.52, found C: 64.42, H: 10.82, N: 7.58. MS *m*/*z*, (%): 186 (M^+, 23), 172 (12), 140 (20), 70 (100).

*(d) 1-Oxyl-trans-3-iodomethyl-4-methyl-2,2,5,5-tetramethylpyrrolidine (**23a**).* Alcohol **22** (450 mg, 2.4 mmol) was converted to mesylate with methanesulfonyl chloride (343 mg, 3.0 mmol) in the presence of Et_3N (303 mg, 3.0 mmol) under the same reaction conditions and procedures as in the case of compound **2**. The crude mesylate and NaI (600 mg, 4.0 mmol) were stirred and refluxed in acetone (15 mL) for 10 h. The reaction mixture was worked up with the same procedures as in the case of compound **3**. After purification with flash column chromatography (hexane/Et_2O), we obtained compound **23a** as an orange oil 426 mg (60%). IR (neat) ν_{max} 2965 cm^{-1}, 2920 cm^{-1}. Anal: calcd. for $C_{10}H_{19}INO$ (296.17), C: 40.55, H: 7.58, N: 4.73, found C: 40.38, H: 7.60, N: 4.63. MS: 296 (M^+, 10), 282 (4), 140 (5), 69 (100).

*(e) 1-Oxyl-trans-3-methanesulfonylthiomethyl-4-methyl-2,2,5,5-tetramethylpyrrolidine (**23b**, reagent V(b)).* The above iodide **23a** (296 mg, 1.0 mmol) and $NaSSO_2CH_3$ (286 mg, 2.0 mmol) in DMSO (8 mL) were heated at 70 °C for 30 min and worked up with the same reaction procedures as in the case of compound **4b**. Purification with flash column chromatography (hexane/EtOAc) yielded compound **23b** as a brown oil 86 mg (31%). IR (neat) ν_{max} 2970 cm^{-1}, 2920 cm^{-1}. Anal: calcd. for $C_{11}H_{22}NO_3S_2$ (280.42), C: 47.12, H: 7.91, N: 4.99, S: 22.87 found C: 47.23, H: 7.90, N: 4.95, S: 22.73. MS *m*/*z*, (%): 280 (M^+, 35), 266 (18), 250 (10), 41 (100).

*Synthesis of V(f) (**25b**, Scheme 3). (a) 1-Oxyl-trans-3-iodomethyl-4-phenyl-2,2,5,5-tetramethylpyrrolidine (**25a**).* Alcohol **24** (993 mg, 4.0 mmol) was converted to mesylate with methanesulfonyl chloride (570 mg, 5.0 mmol) in the presence of Et_3N (505 mg, 5.0 mmol) under the same reaction conditions and procedures as in the case of compound **2**. The crude mesylate and NaI (1.20 g, 8.0 mmol) were stirred and refluxed in acetone (30 mL) for 10 h. The reaction mixture was worked up with the same procedures as in the case of compound **3**. After purification with flash column chromatography (hexane/Et_2O), we obtained compound **25a** as a yellow solid 600 mg (41%); mp 155−156 °C. Anal: calcd. for $C_{15}H_{21}INO$ (358.24), C: 50.29, H: 5.91, N: 3.91. found C: 50.33, H: 5.93, N: 3.97. MS *m*/*z*, (%): 358 (M^+, 4), 344 (6), 216 (10), 56 (100).

*(b) 1-Oxyl-trans-3-methanesulfonylthiomethyl-4-phenyl-2,2,5,5-tetramethyl-pyrrolidine (**25b**, reagent V(f)).* The above iodide **25a** (358 mg, 1.0 mmol) and $NaSSO_2CH_3$ (286 mg, 2.0 mmol) in DMSO (8 mL) were heated at 70 °C for 30 min and worked up with the same reaction procedures as in the case of compound **4b**. Purification with flash column chromatography (hexane/EtOAc) afforded **25b** as a brown solid 136 mg (40%), mp 158−160 °C. Anal: calcd. for $C_{16}H_{24}NO_3S_2$ (342.49), C: 56.11, H: 7.06, N: 4.09, S: 18.72; found C: 56.23, H: 7.10, N: 4.09, S: 18.60. MS *m*/*z*, (%): 342 (M^+, 4), 326 (2), 312 (5), 56 (100).

Scheme 4[a]

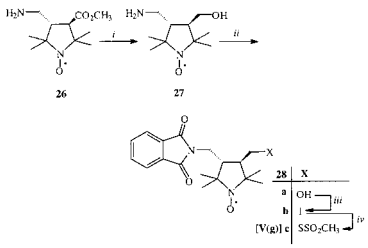

[a] *i*: MeOH, *t*-BuOH, $NaBH_4$, 82 °C, 3 h, 41%; *ii*: phthalimide, Et_3N, toluene, 110 °C, 6 h, 41%; *iii*: (1) MsCl, Et_3N, CH_2Cl_2, 0 °C → r.t., 1 h; (2) NaI, acetone, 55 °C, 20 h, 35%; *iv*: $NaSSO_2CH_3$, DMSO, 70 °C, 30 min, 35%.

*Synthesis of V(g) (**28c**, Scheme 4). (a) 1-Oxyl-trans-3-hydroxymethyl-4-aminomethyl-2,2,5,5-tetramethylpyrrolidine (**27**).* To a stirred solution of ester **26** (2.29 g, 10.0 mmol) and $NaBH_4$ (2.96 g, 80.0 mmol) in anhydr. *t*-BuOH (20 mL), a mixture of anhydr. MeOH (8 mL) and *t*-BuOH (10 mL) was added dropwise over 3 h under N_2. The mixture was worked up with the same procedures as in the case of compound **22.** After purification with flash chromatography ($CHCl_3$/MeOH), we obtained compound **27** as a brown solid 824 mg (41%), mp 125 °C. IR (Nujol) ν_{max} 3310 cm^{-1}, 3250 cm^{-1}. Anal: calcd. for $C_{10}H_{21}N_2O_2$ (201.29), C: 59.67, H: 10.52, N: 13.92; found C: 59.73, H: 10.63, N: 13.97. MS *m*/*z*, (%): 201 (M^+, 23), 187 (10), 157 (11), 41 (100).

*(b) 1-Oxyl-trans-3-hydroxymethyl-4-phthalimidomethyl-2,2,5,5-tetramethyl-pyrrolidine (**28a**).* A suspension of alcohol **27** (804 mg, 4.0 mmol), phthalimide (588 mg, 4.0 mmol), and Et_3N (1.01 g, 10 mmol) in toluene (50 mL) was refluxed in a round-bottom flask equipped with a Dean−Stark apparatus for 6 h. The solvents were evaporated off; the residue was dissolved in $CHCl_3$ (30 mL) and washed with brine (10 mL). The organic phase was separated, dried ($MgSO_4$), filtered, and purified by flash chromatography ($CHCl_3$/Et_2O) to yield compound **28a** as a pale yellow solid 860 mg (41%), mp 189−191 °C. IR (Nujol) ν_{max} 3350 cm^{-1}, 1760 cm^{-1}, 1690 cm^{-1}. Anal: calcd. for $C_{18}H_{23}N_2O_4$ (331.39), C: 65.24, H: 7.00, N: 8.45; found C: 65.16, H: 7.05, N: 8.51. MS: 331 (M^+, 15), 317 (6), 301 (23), 160 (100).

*(c) 1-Oxyl-trans-3-iodomethyl-4-phthalimidomethyl-2,2,5,5-tetramethyl-pyrrolidine (**28b**).* Alcohol **28a** (828 mg, 2.5 mmol) was converted to mesylate with methanesulfonyl chloride (326 mg, 3.0 mmol) in the presence of Et_3N (303 mg, 3.0 mmol) under the same reaction conditions and procedures as in the case of compound **2.** The crude mesylate and NaI (600 mg, 4.0 mmol) were stirred and refluxed in acetone for 20 h. The reaction mixture was worked up with the same procedures as in the case of compound **3**. After purification with flash column chromatography, we obtained compound **28b** as a dark yellow solid 352 mg (35%), mp

Scheme 5[a]

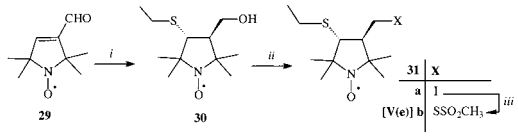

[a] *i:* (1) EtSH, DBU, CH_3CN, r.t., 2 h; (2) EtOH, $NaBH_4$, 0 °C → r.t., 20 min, 50%; *ii:* (1) MsCl, Et_3N, CH_2Cl_2, 0 °C → r.t., 1 h; (2) NaI, acetone, 55 °C, 3 h, 38%; *iii:* $NaSSO_2CH_3$, DMSO, 70 °C, 30 min, 30%.

202−204 °C. IR (Nujol) ν_{max} 1760 cm^{-1}, 1700 cm^{-1}. Anal: calcd. for $C_{18}H_{22}IN_2O_3$ (441.29), C: 48.99, H: 5.02, N: 6.35; found C: 49.00, H: 5.03, N: 6.27. MS: 441 (M^+, 16), 427 (9), 411 (16), 160 (100).

*(d) 1-Oxyl-trans-3-methanesulfonylthiomethyl-4-phthalimidomethyl-2,2,5,5-tetra-methyl-pyrrolidine (**28c**, reagent V(g)).* The above iodide **28b** (220 mg, 0.5 mmol) and $NaSSO_2CH_3$ (134 mg, 1.0 mmol) were heated at 70 °C in DMSO (5 mL) for 30 min and worked up with the same procedures as in the case of compound **4b**. After purification with flash column chromatography ($CHCl_3$/Et_2O), we obtained compound **28c** as a light brown solid 74 mg (35%), mp 140−143 °C. IR (Nujol) ν_{max} 1760 cm^{-1}, 1700 cm^{-1}. Anal: calcd. for $C_{19}H_{25}N_2O_5S_2$ (425.54), C: 53.63, H: 5.92, N: 6.58; found C: 53.73, H: 5.93, N: 6.60. MS: 425 (M^+, 3), 395 (5), 359 (12), 160 (100).

*Synthesis of V(e) (31b, Scheme 5). (a) 1-Oxyl-trans-3-hydroxymethyl-4-ethylthio-2,2,5,5-tetramethyl-pyrrolidine (**30**).* To a solution of aldehyde **29** (1.68 g, 10.0 mmol) and ethanethiol (620 mg, 10.0 mmol) in CH_3CN (20 mL), DBU (152 mg, 1.0 mmol) was added and the mixture was allowed to stand at r.t. for 2 h. The acetonitrile was evaporated off. The residue was taken up in EtOAc (30 mL), washed with 5% aq. H_2SO_4 solution (10 mL) and with brine (10 mL). The organic phase was separated, dried ($MgSO_4$), filtered, and evaporated. The residue (2.0 g) was dissolved in EtOH (20 mL) and $NaBH_4$ (378 mg, 10.0 mmol) was added at 0 °C. The mixture was allowed to stand at r.t. for 20 min. The alcohol was evaporated off; the residue was dissolved in $CHCl_3$ (30 mL) and washed with brine (10 mL). The organic phase was separated, dried ($MgSO_4$), filtered, and purification with flash column chromatography (hexane/EtOAc) yielded **30** as a yellow crystalline solid 1.16 g, (50%), mp 120−122 °C. IR (Nujol) ν_{max} 3370 cm^{-1}. Anal: calcd. for $C_{11}H_{22}NO_2S$ (232.36), C: 56.86, H: 9.54, N: 6.03, S: 13.80; found C: 56.78, H: 9.57, N: 6.00, S: 13.70. MS *m*/*z*, (%): 232 (M^+, 19), 218 (9), 116 (62), 56 (100).

*(b) 1-Oxyl-trans-3-iodomethyl-4-ethylthio-2,2,5,5-tetra-methyl-pyrrolidine (**31a**).* Alcohol **30** (696 mg, 3.0 mmol) was converted to mesylate with methanesulfonyl chloride (400 mg, 3.5 mmol) in the presence of Et_3N (354 mg, 3.5 mmol) under the same reaction conditions and procedures as in the case of compound **2.** The crude mesylate and NaI (900 mg, 6.0 mmol) were stirred and refluxed in acetone (30 mL) for 3 h. The reaction mixture was worked up with the same procedures as in the case of compound **3**. After purification with flash column chromatography (hexane/Et_2O), we obtained compound **31a** as dark yellow solid 390 mg (38%), mp 55−57 °C. Anal: calcd. for $C_{11}H_{21}INOS$ (342.26), C: 38.60, H: 6.18, N: 4.09, S: 9.37; found C: 38.52, H: 6.20, N: 4.08, S: 9.20. MS *m*/*z*, (%): 342 (M^+, 12), 328 (6), 103 (62), 56 (100).

*(c) 1-Oxyl-trans-3-methanesulfonylthiomethyl-4-ethylthio-2,2,5,5-tetramethyl-pyrrolidine (**31b**, reagent V(e)).* The above iodide **31a** (342 mg, 1.0 mmol) and $NaSSO_2CH_3$ (268 mg, 2.0 mmol) were heated at 70 °C in DMSO (8 mL) for 30 min and worked up with the same procedures as in the case of compound **4b**. After purification with flash column chromatography ($CHCl_3$/Et_2O), we obtained compound **31b** as a brown solid 98 mg (30%), mp 40−42 °C. Anal: calcd. for $C_{12}H_{24}NO_3S_3$ (326.51), C: 44.14, H: 7.41, N: 4.29, S: 29.46; found C: 44.18, H: 7.42, N: 4.28, S: 29.50. MS *m*/*z*, (%): 326 (M^+, 9), 312 (5), 232 (10), 56 (100).

Preparation of Spin Labeled T4L Mutants.

Cloning, Expression, and Purification of T4L Mutants. The cloning, expression, purification, and spin labeling of the three T4L mutants investigated (D72C, V131C, and R119C) were previously reported (*4*, *24*). Briefly, overlap extension PCR (*25*) was used to introduce a cysteine at D72, V131, or R119. The entire T4L gene was sequenced by Davis Sequencing (Davis, CA). Mutant plasmids were transformed into *Escherichia coli* BL21 (DE3). Cell cultures were grown to an OD ≈ 1.0, and protein expression was induced by adding IPTG (1 mM). The cells were harvested by centrifugation after 1 h of induction. The cell pellets were resuspended in a buffer containing 25 mM Tris, 25 mM MOPS, and 0.2 mM EDTA, pH 7.6, and sonicated for 4 min on ice (output 4, duty cycle 50% using a Branson Sonifier 250 and a standard disruption horn). The cell debris was pelleted by centrifugation at 27000*g* for 15 min. The supernatant was filtered (0.2 μ) and loaded onto a Resource S cation-exchange column equilibrated with the same buffer. T4L was eluted with a linear NaCl gradient (from 0 to 1.0 M NaCl). Protein purity was determined to be 95% pure on a 15% SDS−PAGE gel.

Spin Labeling of T4L Mutants. Immediately before spin labeling, the protein was exchanged into a suitable buffer (50 mM MOPS and 25 mM NaCl at pH 6.8) using a Hi-Trap desalting column. The T4L mutants (typically ≈ 1 μM) were incubated with 10-fold molar excess of the desired spin labeling reagent. The reaction was allowed to proceed at room temperature for at least 1 h. For the hydrophobic reagents I(f) and V(f), the formation of a precipitate was noted for incubations longer than 1 h. A Hi-Trap desalting column was used to remove excess spin label, and protein solutions were concentrated to 200 μM using a Microcon filter concentrator (10 kD cutoff).

The spin labeled mutants are designated by the residue number at which the nitroxide is introduced, and the code for the side chain given in Figure 1. For example, 72R1(a) is a mutant with the R1(a) side chain at site 72.

EPR of Spin Labeled T4L Mutants.

EPR Measurements. EPR spectroscopy was performed on a Varian E-109 spectrometer fitted with a two-loop one-gap resonator (*26*). Protein samples of 5 μL (∼200 μM) were loaded in Pyrex capillaries (0.84 mm o.d. × 0.6 mm i.d.) sealed on one end. All spectra were acquired using a 2 mW incident microwave power and ca. 1 G field modulation amplitude at 100 kHz. To reduce the rotary diffusion rate of the protein, all spectra were recorded in 30% w/v sucrose (*4*). Sucrose at this concentration does not affect the rotational

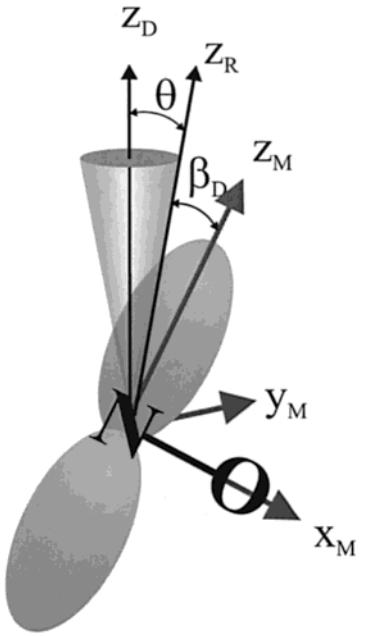

FIGURE 3: A diagram showing the relationship between the nitroxide magnetic frame (z_M, y_M, and x_M), the *z*-axis of the diffusion tensor (z_R), and the protein fixed director (z_D) taken to lie along the symmetry axis of the ordering potential. The angle β_D defines the fixed tilt of z_R with respect to z_M. The angle θ is the instantaneous angle between z_R and z_D. Over time, z_R moves within a space defined by the ordering potential.

mobility of the side chain (*27*). The EPR spectra of some samples had small (<5%) contributions from free spin label in solution. In these cases, the free component was removed by subtraction (*28*).

Simulations of EPR Spectra. Experimental EPR spectra were fit to the MOMD model of Freed and co-workers (*29*) using a modified Levenberg−Marquardt algorithm (*29*, *30*). The paper of Budil et al. (*30*) provides a detailed description of the model, simulation parameters and fitting procedures. A brief description specific to the implementation used in the present work is given below. For consistency, the notation used is that of Budil et al. (*30*).

In the MOMD model, three coordinate frames are employed to represent the internal motion of the nitroxide in the protein, as illustrated in Figure 3. The first is the molecule-fixed magnetic tensor frame (x_M, y_M, z_M). As is customary, z_M lies along the nitroxide p orbital, x_M lies along the NO bond axis, and y_M is selected for a right-handed coordinate system. The magnetic frame is the principal frame for both the nitroxide hyperfine (**A**) and **g** tensors. The second coordinate frame is the principle frame of the rotational diffusion tensor (x_R, y_R, z_R). In general, the rotational diffusion and magnetic frames are not coincident. The relationship between these frames is specified by the diffusion tilt angles (α_D, β_D, γ_D), defined as the Euler angles required for rotation of the magnetic frame into the diffusion frame. Simulations of the experimental spectra to be discussed below are strongly dependent on β_D, the tilt angle between z_R and z_M (Figure 3), but weakly dependent on α_D and α_D. Anisotropic motions are simulated in the MOMD model by introducing a restoring (ordering) potential (U) that constrains the spatial extent of the motion of z_R. As will be shown below, the spectra of R1(x) in T4L are adequately described by the restoring potential $U(\theta) = -1/2k_BTc_0^2(3\cos^2\theta - 1)$, where c_0^2 is a scaling coefficient and θ is the (instantaneous) angle between z_R and the symmetry axis of the potential. The symmetry axis of the potential defines the *z*-axis of the third and final coordinate frame, the director frame. For describing the nitroxide side chains on a protein subject to the above ordering potential, the director frame is uniaxial (z_D) and fixed in the protein. The existence of the restoring potential results in an anisotropic motion and can be characterized by the order parameter $S = -1/2\langle(3\cos^2\theta - 1)\rangle$, where the brackets indicate spatial average. For an individual protein molecule, z_D forms an angle ψ with respect to the external magnetic field. To obtain the final spectrum corresponding to an isotropic distribution of protein orientations, the spectra are summed over ψ.

For fitting of experimental spectra of 72R1(a) to the MOMD model, published values for the elements of the **A** and **g** tensors (A_{xx}, A_{yy}, A_{zz} and g_{xx}, g_{yy}, g_{zz}) for R1(a) on exposed sites of T4L were used as starting values (*6*). The fit was then optimized with the rotational diffusion rates (R_{xx}, R_{yy}, R_{zz}), the coefficient of the ordering potential (λ_o), and the diffusion tilt angles (α_D, β_D, α_D) as parameters. Next, all parameters were optimized by a global fit of the spectrum to both X- and Q-band spectra. The final values of the **A** and **g** tensor elements (Table 1, legend) were very similar to the previously published values and were used as constants in all other simulations.

For comparative purposes, EPR spectra were also simulated using the effectiveHamiltonian model previously described (*31*). In the effective Hamiltonian model, the Hamiltonian is time-independent, and the principle values of the **A** and **g** tensors are taken as spatial averages corresponding to the range of motion under consideration (*32*). Axial anisotropic motion is completely characterized by the order parameter $S = -1/2\langle(3\cos^2\theta - 1)\rangle$, where θ is the angle between the symmetry axis of the anisotropic motion (z_D) and z_R.

RESULTS

Analysis of Side Chain Motion at Site 72. (a) Motion of 72R1(a): the 4-H Parent of Series 1. The EPR spectrum of 72R1(a) at 21 °C is shown in Figure 4, panel A. This general line shape, with well-resolved hyperfine extrema (arrows), was first observed in spin labeled lipids and shown to be characteristic of anisotropic rotation of the nitroxide (*31*−*33*). The dashed line superimposed on the experimental spectrum is the best fit simulation using the MOMD model. The parameters of the simulation are given in Table 1. The principle values of the **g** and **A** tensors are similar to those for R1(a) determined at 250 GHz at solvent-exposed sites in T4L (*6*). According to the best fit simulation, $\beta_D = 36°$ and $S = 0.47$. The simulated spectral line shapes are relatively insensitive to α_D and insensitive to γ_D, which was set to zero for all simulations.

As is well-known, it is difficult to unambiguously resolve contributions from diffusion rates (R_{xx}, R_{yy}, R_{zz}) and order (S) using simulations of spectra at a single frequency (*34*). That is, sets of these parameters determined from fitting procedures are not unique. For instance, a simulation with low rates and a low order parameter can generate a similar spectrum to that of one with a higher order parameter and

Table 1: Dynamic Parameters for EPR Simulations[a]

residue	spin label	T (°C)	R_{xx} ($\times 10^7\,s^{-1}$)	R_{yy} ($\times 10^7\,s^{-1}$)	R_{zz} ($\times 10^7\,s^{-1}$)	S	c_0^2	α_D (deg)	β_D (deg)
72	R1(a)	21.0	9.77	6.31	7.41	0.47	2.15	4	36
72	R5(a)	21.0	9.77	6.31	7.41	0.47	2.15	15	99
131	R1(a)	21.0	9.77	6.31	7.41	0.35	1.59	4	36
131	R5(a)	21.0	9.77	6.31	7.41	0.35	1.59	15	99

[a] The magnetic parameters used for all simulations are as follows: $g_{xx} = 2.0076$, $g_{yy} = 2.0050$, $g_{zz} = 2.0023$, and $A_{xx} = 6.2$, $A_{yy} = 5.9$, $A_{zz} = 37$.

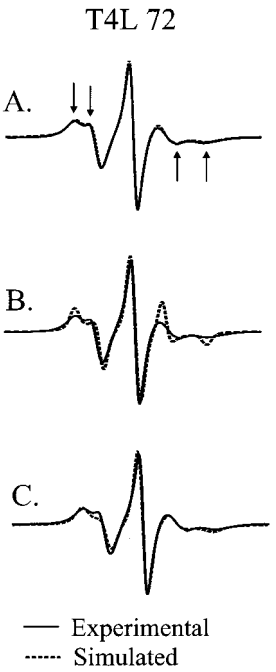

FIGURE 4: The experimental EPR spectrum of 72R1(a) (solid line) superposed with simulated spectra (dashed lines) according to the MOMD (panel A), effective Hamiltonian (panel B), and the modified effective Hamiltonian (panel C) models. The arrows in panel A mark the hyperfine extrema characteristic of the anisotropic spectrum. The effective Hamiltonian spectrum was calculated as described previously using a manifold independent Lorentzian linewidth of 3.2 G (with $S = 0.43$) (*31*). The modified effective Hamiltonian spectrum was calculated in the same way but using manifold dependent Lorentzian linewidths determined using Redfield theory (*35*).

higher rates. To explore the limits of the "order/rate" uncertainty, a library of fits was generated by varying the order parameter about $S = 0.47$ and optimizing the rates to compensate for the spectral changes. Acceptable fits can only be obtained for S in the range 0.47−0.53 and for log R_{xx}, log R_{yy}, and log R_{zz}, in the ranges 7.95−8.05, 7.70−7.90, and 7.80−7.90, respectively (data not shown). Thus, there is some uncertainty in the values of S and the R's, but the ordering potential is essential for an adequate fit. Even small (± 5°) changes in β_D have a pronounced effect on the spectrum that cannot be compensated for by changes in R or S values (data not shown).

The diffusion rates estimated from MOMD simulations correspond to rotational correlation times of ≈ 2 ns at 21 °C. This approaches the fast motional regime, where an effective Hamiltonian treatment for anisotropic motion should give an approximate fit to the spectra (*31*, *32*). Figure 4, panel B, shows that the fit to the effective Hamiltonian is an adequate representation of the positions of spectral turning points, but that the widths of the $m_I = -1$ and +1 resonance lines are too narrow as compared with the experimental spectrum. This is due to the neglect of rate effects, which can be accounted for by including a nuclear state-dependent linewidth calculated from Redfield relaxation theory (*35*). Figure 4, panel C, shows the improvement realized by an approximate treatment where the relative linewidths are computed for a 2 ns isotropic correlation time according to Gaffney and McConnell (*35*).

To determine whether new modes of motion are excited by an increase in temperature or whether weak interactions could be detected with a decrease in temperature, the temperature dependence of the 72R1(a) spectrum was investigated in the range of 4−40 °C. Figure 5, panel A, shows representative spectra in this temperature range. The characteristic anisotropy, indicated by resolved parallel and perpendicular components of the **A** tensor (see arrows, Figure 4), is retained up to about 34 °C, indicating that no fundamental changes in geometry of the motion take place. Above 34 °C, the nitroxide magnetic anisotropy is mostly averaged.

The experimental spectra can be simulated reasonably well with the same anisotropic model for the motion by simply increasing the rates with increasing temperature. The dashed traces in Figure 5, panel A, are simulated spectra obtained by fixing all parameters other than R_{xx}, R_{yy}, and R_{zz}. Figure 5, panel C, shows an Arrhenius plot of the average rate $\langle R \rangle = [(R_{xx}R_{yy}R_{zz})^{1/3}]$ determined from the simulations in the temperature range 4−40 °C. The data fit a straight line with a slope corresponding to an apparent activation energy of ≈ 6 kcal/mol. This is an upper boundary to the activation energy, because temperature-dependent changes in the order parameter could contribute to some extent to the changes in line shape.

(b) Motion of 72R1(b): The Effect of a 4-CH_3 Substituent in Series 1. Figure 5, panel B, shows the EPR spectra of 72R1(b) at representative temperatures in the range of 4−39° C. In previous work, the 4-methyl substituent in R1(b) was shown to reduce the mobility of the nitroxide relative to R1-(a) when compared at helix surface sites in T4L at room temperature (*4*). The large magnitude of the effect can be appreciated by comparing the spectra of 72R1(a) in Figure 5, panel A, with those at similar temperatures for 72R1(b) in Figure 5, panel B. In each case, the much larger separation of the outer hyperfine extrema in 72R1(b) indicates a lower mobility.

To examine the origin of this effect, simulations of the 72R1(b) spectra were carried out, and the results are shown as dotted traces superposed on the experimental spectra in Figure 5, panel B. An important outcome of the simulations is that good fits are obtained for the spectra as a function of temperature at a constant order parameter with variation of rates alone, just as for the case of 72R1(a). However, the order parameter required for fits to the 72R1(b) spectra in

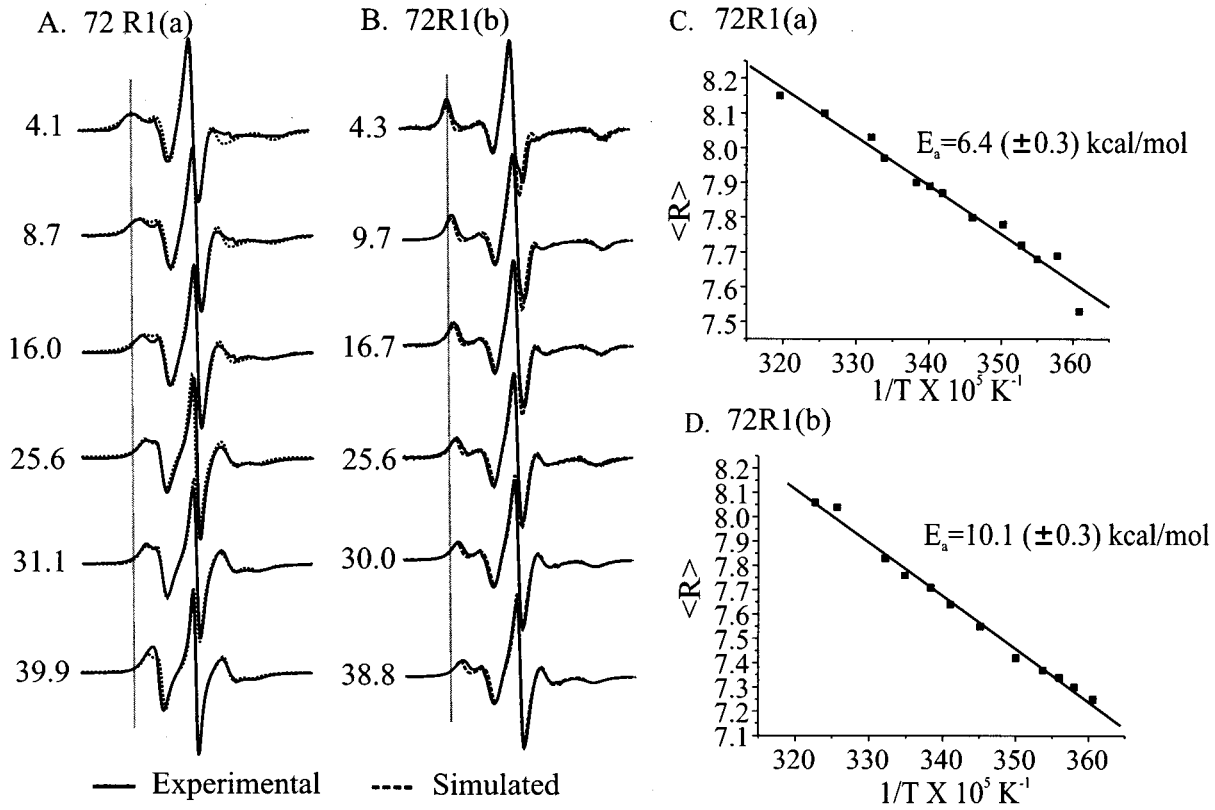

FIGURE 5: The MOMD simulated (dashed lines) and experimental (solid lines) spectra of 72R1(a) (A) and 72R1(b) (B) are shown at temperatures ranging from 4 to 40 °C. The gray vertical lines are drawn as references to guide the eye for comparison. Only R_{xx}, R_{yy}, and R_{zz} were varied for each temperature. Arrhenius plots for 72R1(a) and 72R1(b) are shown in panels C and D, respectively. The activation energy, E_a, was calculated from the slope of the line. The error calculated from the standard deviation is shown in parentheses.

Figure 5, panel B, is $S = 0.81$, rather than $S = 0.47$ that was required for fits to the 72R1(a) spectra. The apparent increase in order parameter due to the presence of the 4-CH_3 substituent corresponds to a decrease in the RMS angle of deviation of z_R (θ in Figure 3) from $\approx$ 37 to 20°. Thus, within the context of the MOMD model, the 4-CH_3 substituent significantly restricts the amplitude of motion of z_R and the nitroxide. Modeling suggests that the effect arises from steric constraints on bond rotations within the side chain due to the methyl group, as discussed below.

Figure 5, panel D, shows an Arrhenius plot of the average rates $\langle R \rangle = [(R_{xx}R_{yy}R_{zz})^{1/3}]$ determined from simulation of temperature-dependent spectra of 72R1(b), including the examples shown in Figure 5, panel B. The apparent activation energy of $\approx$ 10 kcal/mol is approximately 4 kcal/mol greater than that for 72R1(a). Thus, in addition to increasing the order parameter, the 4-CH_3 substitutent in 72R1(b) increases the activation barrier for the dynamic mode that produces spectral averaging.

(c) Motion of 72R1(c−g): The Effect of Increasing Size of the 4-Substituent in Series 1. Although the introduction of the 4-methyl group resulted in an increase in order, the order parameter of 72R1(b) is still less than unity, due to either residual bond oscillations within the side chain, backbone fluctuations, or both. If residual bond rotational modes contribute, increasing the size of the 4-substituent might further increase the order. To investigate this point, the series of side chains of increasing size and varying degrees of polarity, designated R1(x) in Figure 1, were introduced at site 72 in T4L. The corresponding EPR spectra at 19 °C are shown in Figure 6, panel A, along with the best fits with varying S. For simplicity, the diffusion rates were fixed for all simulations. The fits using this model are generally satisfactory for all but the large polar substituent 72R1(g). However, the central linewidths and the values of the maximum hyperfine splitting ($2A'_{zz}$ in Figure 6, panel A) are slightly underestimated, suggesting that the 4-substituents do reduce the rate to some extent or that there are small geometrical changes in the side chain. For the bulky 72R1(g), a good fit cannot be obtained without a reduction in the rates of motion as well as an increase in order parameter relative to 72R1(a).

Figure 6, panel B, shows the RMS values of θ ($\langle\theta\rangle$) for the derivatives, excluding 72R1(g), corresponding to the order parameters obtained from the MOMD fits of Figure 6, panel A (solid bars). As can be seen, $\langle\theta\rangle$ decreases sharply for the addition of the first carbon atom at the 4-position of the ring [i.e., the -CH_3 group in R1(b)]. Thereafter, further increases in the molecular weight of the substituent produce small but significant additional decreases in $\langle\theta\rangle$. A similar trend is seen in the value $\langle\theta\rangle_{apparent}$ (Figure 6, panel B, open bars) calculated from the apparent order parameter derived directly from the hyperfine splittings of the experimental spectra (*31*). Although $\langle\theta\rangle$ for the side chain 72R1(g) is not included in Figure 6, panel B, due to the poor fit, the value of $\langle\theta\rangle_{apparent}$ derived from the experimental spectrum follows the general trend of decreasing angular deviation with increasing bulk of the substituent.

The spectra of 72R1(f) and 72R1(g) are both characteristic of strongly immobilized nitroxides. For 72R1(g), the splitting of the outer hyperfine extrema is $\approx$ 68 G, as compared to the maximum value in aqueous media in the absence of

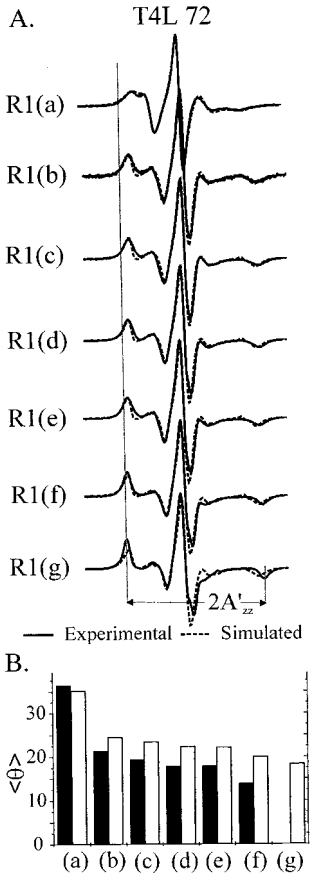

FIGURE 6: The EPR experimental spectra for 72R1(a−g) (solid lines) and the corresponding MOMD simulations (dashed lines) are compared in panel A. The gray vertical line is drawn as a reference to guide the eye for comparison. For the simulations, the ordering potential was varied for each substituent, while the rates were fixed (log $R_{xx} = 7.96$, log $R_{yy} = 7.78$, and log $R_{zz} = 7.85$). The angle $\langle\theta\rangle$ was calculated from the order parameter for the best fit in R1(a−f) (panel B, solid bars) and $\langle\theta\rangle_{apparent}$ was calculated from $2A'_{zz}$ of the experimental spectra R1(a−g) (panel B, open bars) (*31*).

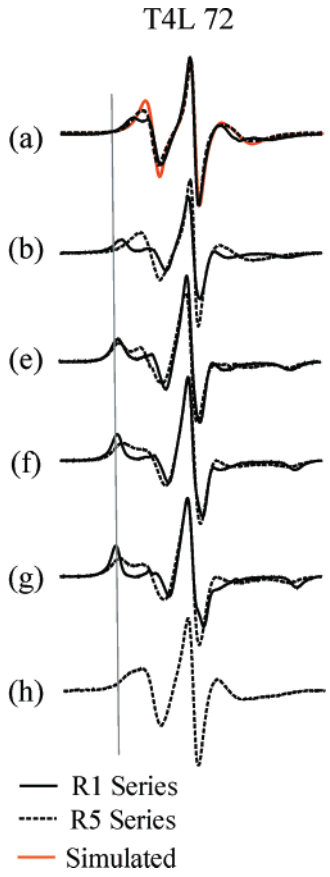

FIGURE 7: The spectra of 72R1(a−g) (solid lines) are compared to the spectra of 72R5(a−h) (dashed lines). The MOMD simulated spectrum of 72R5(a) is displayed with a red line. The gray vertical line is drawn as a reference to guide the eye for comparison.

motion of ≈ 74 G (*36*). If 72R1(g) is indeed completely immobilized relative to the protein, the correlation time determined from the spectrum should reflect the rotational motion of the protein itself. Using a Brownian diffusion model and a 3.0 G intrinsic linewidth, the correlation time of the nitroxide in 72R1(g) is estimated to be $\tau_{nitroxide} \approx 17$ ns (*37*). This is indeed close to the rotational correlation time for T4L in 30% sucrose ($\tau_{T4L} \approx 18$ ns) estimated from the Stokes−Einstein equation. Similar results are obtained for 72R1(f), although there is slightly more motion relative to 72R1(g) ($(2A'_{zz} \approx 66.7$, $\tau_{nitroxide} \approx 13$ ns). Thus, the 72R1(g) side chain is effectively immobilized relative to the protein, and the 72R1(f) side chain is nearly so. For these bulky 4-phenyl and 4-pthalidimido derivatives, the immobilization likely reflects direct interaction of the substituent with the protein environment.

(d) Motion of 72R5(x): The Effect of Nitroxide Ring Geometry. The 5-series of nitroxide side chains are saturated analogues of the 1-series (Figure 1), the sole difference being a change in hybridization of the 3 and 4 carbon atoms of the ring from sp^2 to sp^3. Substituents at the 3- and 4-positions are known to be in the trans configuration because of the synthetic route by which they were obtained (*22*). The spectrum of 72R5(a) in T4L has been previously reported (*5*) and is reproduced in Figure 7 for comparison with 72R1-(a). As can be seen, there is much more effective averaging of the magnetic anisotropy in 72R5(a) as compared to 72R1-(a). The spectrum of 72R5(a) can be simulated by a simple change in the orientation of the diffusion tensor ($\beta_D = 99°$) relative to that in 72R1(a) ($\beta_D = 36°$), without changes in the rates (Figure 7, red trace; Table 1). However, the line shape of 72R5(a) is less sensitive to changes in β_D than 72R1-(a) and a range between 80 and 120° produces reasonable fits (data not shown).

Remarkably, in the 72R5(x) series, introduction of a trans 4-CH_3 substituent (72R5(b)) produces relatively little change in the EPR spectrum and hence in side chain motion. This is to be compared with the dramatic immobilization of 72R1-(b) due to the 4-CH_3 (Figure 7, trace b). Although the R1(h) side chain with a 4-$CONH_2$ substituent has not been prepared, the results presented in Figure 7 leave little doubt that it would be at least as immobilized as R1(b) at site 72 in T4L. In contrast, the spectrum of 72R5(h) suggests a mobility nearly as high as 72R5(a) itself (Figure 7, trace h). Thus, for the relatively small substituents -CH_3 and -$CONH_2$, the constraint imposed on motion in the series 1 side chains is removed in the saturated analogues of series 5. For 72R5-(e)-72R5(g), the substituent results in strong immobilization relative to 72R5(a) but less than that produced by the same substituent in the 72R1(x) series (Figure 7, traces e−g).

Analysis of Side Chain Motion at Site 131. As will be shown below, the spectrum of 131R1(a) at room temperature reflects an anisotropic motion of a single component that

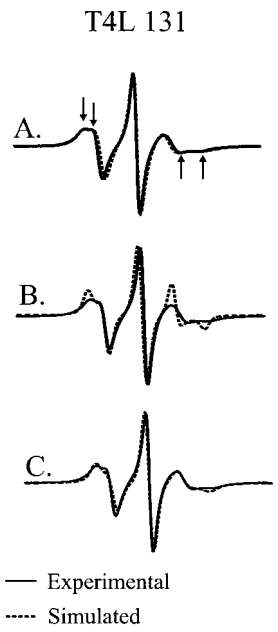

FIGURE 8: The experimental EPR spectrum of 131R1(a) (solid line) superposed with simulated spectra (dashed lines) according to the MOMD (panel A), effective Hamiltonian (panel B), and the modified effective Hamiltonian (panel C) models. The arrows in panel A mark the hyperfine extrema characteristic of the anisotropic spectrum. The effective Hamiltonian spectrum was calculated as described previously using a manifold independent Lorentzian linewidth of 2.9 G (with $S = 0.32$) (*31*). The modified effective Hamiltonian spectrum was calculated in the same way but using manifold dependent Lorentzian linewidths determined using Redfield theory (*35*).

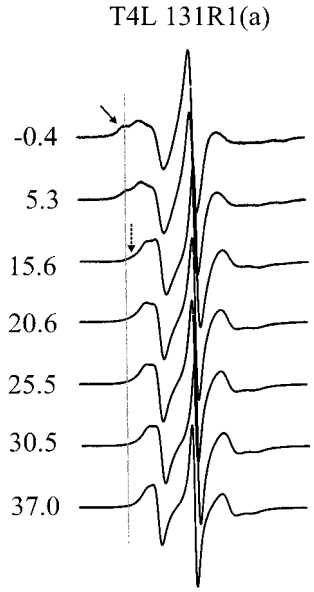

FIGURE 9: The experimental EPR spectra of 131R1(a) at temperatures ranging from −0.4 to 37 °C. The dashed arrow points to a shoulder corresponding to small population of a second spectral component at 15.6 °C, and the solid arrow indicates a resolved population of the second spectral component at −0.4 °C. The gray vertical line is drawn as a reference to guide the eye for comparison.

can be directly compared with that of 72R1(a). However, at reduced temperature or with 4-substituents, interactions of the nitroxide at 131 with nearby groups in the protein are evident in complex EPR spectra. For these cases, spectral simulations are not attempted, and the analysis is qualitative.

(a) Motion of 131R1(a): The 4-H Parent of Series 1. The spectrum of 131R1(a) in T4L at room temperature was previously obtained (*4*) and is reproduced in Figure 8, panel A. Like the spectrum of 72R1(a), the line shape is characteristic of anisotropic motion but with more closely spaced (and less well-resolved) hyperfine extrema (arrows). Accordingly, a good fit to the spectrum is obtained with the same parameters used for 72R1(a), except with a lower order parameter of 0.35 rather than 0.47 (Figure 8, panel A; Table 1). This amounts to a difference of $\Delta\langle\theta\rangle \approx 5°$ in the RMS angle of deviation of the diffusion z_D axis, being greater for 131R1(a). Simulations using the same order parameter as 72R1(a) but with different rates were less satisfactory (data not shown).

As for 72R1(a), the spectrum of 131R1(a) can be approximately accounted for with an effective Hamiltonian (Figure 8, panel B) but with a reduced apparent order parameter as compared to 72R1(a). Again, the effective Hamiltonian approach reproduces the spectral turning points but not the linewidths, and the fit is substantially improved by approximate corrections for rate effects, as for 72R1(a) (Figure 8, panel C).

Figure 9 shows the spectrum of 131R1(a) at various temperatures. Like 72R1(a), the features of the spectrum characteristic of an anisotropic motion are observed throughout the temperature range investigated. However, unlike 72R1(a), a second, less mobile component is resolved at lower temperatures (indicated by the arrow in Figure 9). At −0.4 °C, the populations of the two states are of the same order of magnitude. At higher temperature, the less mobile component is decreased in amplitude and is no longer resolved but is evident in the broad low-field tail of the spectrum up to about 15.6 °C (dashed arrow in Figure 9). Apparently, the nitroxide in 131R1(a) is in proximity to groups in the protein with which it can favorably interact, but the interaction is sufficiently weak that it is detected in the EPR spectrum only at reduced temperature. At room temperature, thermal energy effectively competes with the interaction(s). Further evidence for the interaction is provided below.

(b) Motion of 131R1(b−g): The Effect of 4-Substituents in Series 1. Qualitatively, the effect of the 4-substituent on the spectrum of 131R1(x) is similar to that of 72R1(x), that is, an increase in substituent size leads to a decrease in mobility, as judged by the regular increase in the splitting of the hyperfine extrema and the central linewidth in the spectra of Figure 10. However, unlike the case for 72R1(x), the spectra of 131R1(x) cannot be satisfactorily simulated assuming a single population of spins. In general, the high and low field extrema of the experimental spectra are broader than can be obtained with a single population of spins with the anisotropic motion that characterizes 131R1(a). An example of the poor fit quality is shown by the dashed trace in Figure 10 for 131R1(c). The additional broadening in the spectra could arise from a distribution of mobility states due to weak interaction of the 131R(x) substituents with the environment in the protein. This possibility is suggested by the data of Figure 9, where an interaction of 131R1(a) with the environment is detected at low temperature. The larger substituents of the b−g derivatives would have stronger interactions whose effects are reflected at room temperature.

As shown above, the mobility of 131R1(a) is apparently

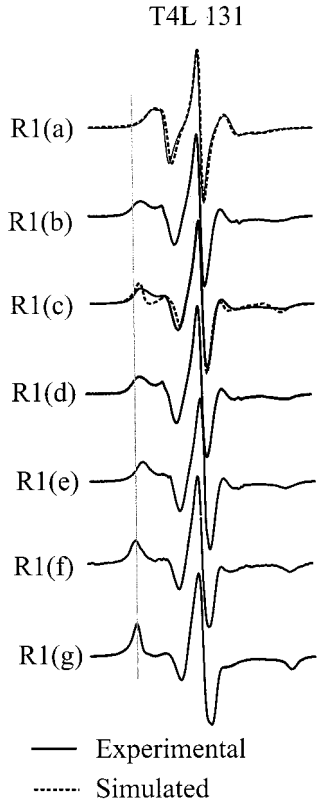

FIGURE 10: The experimental EPR spectra of 131R1(a−g) (solid lines) and the MOMD simulated spectra of 131R1(a and c) (dashed lines). The gray vertical line is drawn as a reference to guide the eye for comparison.

greater than that for 72R1(a), as judged by a reduced order parameter for the former. Similarly, the mobility of each 4-substituted derivative in the 131R1(x) series is generally more mobile than the corresponding 72R1(x) derivative (compare the solid lines of Figure 10 to those of Figure 6, panel A). However, the differences are subtle, and the comparison is complicated by the possibility of interactions of the 4-substituents with the environment in the case of 131R1(x).

Temperature Dependence of 119R1(a). The results presented in Figure 9 suggest that R1(a) at site 131 can interact with its environment, giving rise to two resolved components in the spectra at reduced temperature, one of which is relatively immobilized. The appearance of two resolved components in the EPR spectra was previously observed in a number of spin labeled mutants of T4L at room temperature, including 119R1(a) (*5*). In the case of 119R1(a), the crystal structure of the spin labeled protein clearly shows that the two spectral components arise from two rotamers of the side chain, one of which is immobilized by interaction with nearby side chains (*10*). Here, 119R1(a) is used as a model system to examine the temperature dependence of the interactions that give rise to the two states for comparison with 131R1(a). The spectrum of 119R1(a) is shown in Figure 11. At 24 °C, two spectral components are resolved, and the populations of the two mobility states are roughly equal. As the temperature is increased, the population of the immobile component (β in Figure 11) is apparently decreased, and by $\approx$ 40 °C is no longer detectable. As the temperature is reduced from 24 °C, the immobile component grows to become a dominant population near 0 °C.

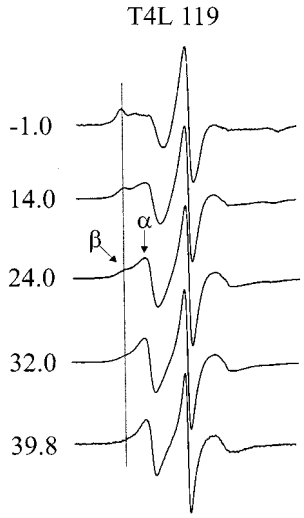

FIGURE 11: EPR spectra of 119R1(a) at temperatures ranging from −1.0 to 40 °C. Two spectral components are labeled α (mobile component) and β (immobile component). The gray vertical line is drawn as a reference to guide the eye for comparison.

DISCUSSION

A specific objective of the present study is to evaluate in the simple X_4/X_5 model for internal motion of the R1(a) side chain on solvent-exposed surfaces of α-helices using 72R1-(a) as a reference. As discussed in detail in the paragraphs to follow, spectral simulations and the effects of 4-substitution and changes in ring geometry all support the simple model. Given this result, preliminary studies of the effects of backbone motion and tertiary interactions on side chain motion are discussed.

Internal Motion of the R1(x) Side Chains and the Molecular Origin of the 4-Substituent Effect. (a) Simulations Support the X_4/X_5 Model. Spectral simulations provide the most powerful tool for elucidating the dynamic mode of the nitroxide in a spin labeled side chain. Unfortunately, a direct comparison between the parameters obtained from simulations and the molecular X_4/X_5 model is not straightforward. This is because the simulations represent the overall motion as diffusion about three mutually perpendicular axes independent of the molecular model, while the actual motion corresponding to the physical model is rotation about two bond axes that intersect at the tetrahedral angle. Nevertheless, it is possible to identify an approximate correspondence between the parameters of the simulation and the X_4/X_5 model that suggests their mutual compatibility. To appreciate this, recall that the simulations indicate an anisotropic motion with relatively unrestricted diffusion about a z_R axis that makes an angle of $\approx$ 36° with respect to the nitroxide p orbital and restricted diffusion about axes perpendicular to z_R. A energy-minimized model of the side chain based on the crystal structures reveals that the rotation axes of X_4 and X_5 correspond roughly to the principle diffusion axes identified by the simulation (Figure 12, panel A). Thus, the axis of X_4 makes an angle of $\approx$20−30° with the molecular z_M axis, lying approximately parallel to the z_R diffusion axis. The rotation axis of X_5 lies in the x_M, y_M plane and may be taken to correspond approximately to a principle diffusion axis perpendicular to z_R. Moreover, the molecular rotation about X_4 is relatively unhindered, while that about X_5 is confined by a potential arising from interactions of the S_δ

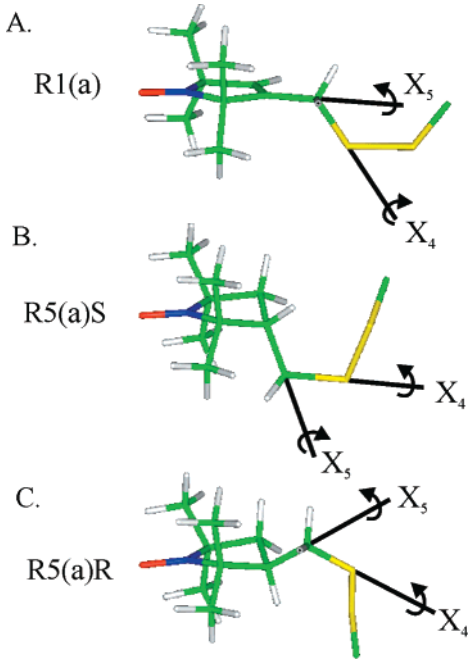

FIGURE 12: Stick models of the nitroxide side chains R1(a) (panel A), R5(a)S (panel B), and R5(a)R (panel C), where S and R denote the stereochemistry of carbon 3 in the nitroxide ring. The axes of bond 4 and 5 are extended and labeled with the corresponding dihedral angles.

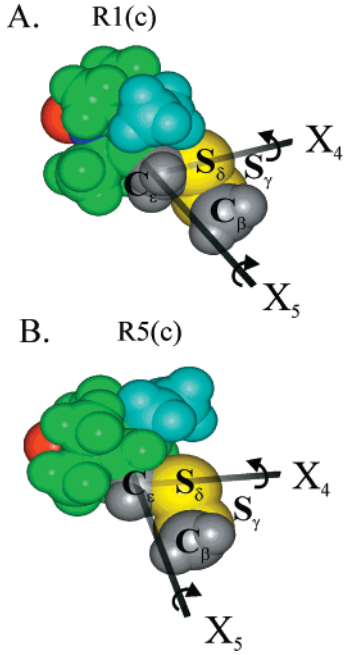

FIGURE 13: CPK models of R1(c) and R5(c) with the side chain atoms labeled. The axes of bond 4 and 5 are extended and labeled with the corresponding dihedral angles. The 4-substituent (-CH_2-CH_3) is shown in blue, the nitroxide oxygen in red, the nitrogen in blue, and other nitroxide ring atoms in green.

of the disulfide with the α-methyl groups and the 4-H of the nitroxide ring. This potential may be identified with the restoring potential of the MOMD simulations and the corresponding order parameter. Thus, the parameters of the simulation correspond approximately with molecular motions predicted from the X_4/X_5 model. A key point is that the hindered rotation about X_5, due to the 4-H and the ring methyl groups, gives rise to the molecular ordering reflected by the order parameter.

(b) The Effect of 4-Substituents Can Be Understood by the X_4/X_5 Model. The addition of a 4-substituent in the nitroxide ring of series 1 causes a striking reduction in mobility. As shown in Figure 6, the changes in the EPR spectra due to a variety of substituents in 72R1(x) can be simulated by a simple reduction in order parameter relative to that of 72R1(a). As discussed above, an increase in order parameter should correspond to a reduction in the amplitude of oscillation of X_5 brought about by the substituent. Molecular models of the R1(x) side chain show that this is indeed the case (Figure 13, panel A). A 4-substituent (blue) on the nitroxide ring hinders rotational about X_5 due to a steric clash of the substituent with S_δ of the disulfide, thus accounting for the increase in the order parameter by the substituent.

Interestingly, the first atom in the linear substituent series R1(a)−R1(d) is the most effective in reducing the angle of oscillation (Figure 7, trace b). Thus, the -CH_3 group of 72R1(b) reduces the RMS angle of oscillation by $\Delta(\langle\theta\rangle) \approx -15°$ relative to R1(a). Additional increases in the substituent size produce only small incremental changes of $\Delta(\langle\theta\rangle) \leq -5°$ relative to R1(b). Again, the X_4/X_5 model offers an explanation for this effect, because the first atom in the substituent is the determinant of the steric interaction with the S_δ atom, thereby modulating motion of X_5. Additional atoms in a linear substituent simply project outward away from the sulfur (Figure 13, panel A).

In 72R1(f) and 72R1(g), the bulky substituent leads to complete immobilization of the nitroxide. Because of the size of these substituents, direct interactions with surrounding groups in the protein structure are likely, and the effect cannot be interpreted solely in terms of steric influence on bond rotations.

(c) The Temperature Dependencies of 72R1(a) and 72R1-(b) EPR Spectra Are Consistent with Activation of X_5 Torsional Oscillations. As shown in Figure 5, the temperature dependencies of the rates for 72R1(a) and 72R1(b) exhibit simple Arrhenius behavior with apparent activation energies of ≈ 6 and ≈ 10 kcal/mol, respectively, in 30% sucrose. These are the activation energies for the dynamic processes giving rise to spectral averaging, and in the context of the X_4/X_5 model, these are rotations about bonds 4 and 5. The fact that the 4-CH_3 substituent in 72R1(b) increases the activation energy by more than 50% strongly supports this model and points to rotation about bond 5 as the major contributor to spectral averaging.

It is instructive to compare the above activation energies with predictions for diffusive processes in solution and with other relevant experimental values in the literature. For example, the activation energy for simple rotary diffusion in a viscous medium is close to E_η, the activation energy for viscous flow of the solvent (*38*). For 30% sucrose, $E_\eta \approx$ 6 kcal/mol, as computed from the temperature dependence of viscosity (*39*). This is a lower limit for the activation energy expected for rotational diffusion in the tethered nitroxide side chain, assuming that the side chain is normally solvated. Because the activation energies for solvent flow and side chain internal motion in 72R1(a) are similar, internal barriers to rotation must be small. A quantitative analysis (*40*) gives the experimental activation energy for bond rotary diffusion (E_{exp}) as $E_{exp} = E_\eta + E_i$, where E_i is the internal

activation energy for bond rotation. Thus, the internal activation energy for the bond rotation(s) giving rise to the spectral averaging for 72R1(a) in 30% sucrose is $E_i \approx 0$. Thus, torsional oscillations about X_5, constrained by the restoring potential, are essentially damped only by solvent interactions. A similar conclusion was reached for the rotational motion of a nitroxide side chain in poly(methacrylamide)-type copolymers in methanol (*41*). In addition, the experimentally determined activation energy for torsional oscillations about the C-C bonds in lysine side chains in water has been reported to be ≈ 4 kcal/mol (*42*). Subtraction of $E_\eta \approx 4$ kcal/mol for water gives $E_i \approx 0$, similar to that deduced above for rotations in the R1(a) side chain. For 72R1(b), $E_i \approx 4$ kcal/mol, presumably arising from the additional interaction of the -CH_3 group with S_δ of the side chain. This value is in the range observed for nitroxide side chain rotations in sterically constrained environments in polymers. For example, Bullock and Cameron (*40*) report an E_i for nitroxide rotations in spin labeled polystyrene in cyclohexane of 3.5 kcal/mol. Moreover, they noted an increase in E_i of ≈ 1 kcal/mol due to the addition of an α-CH_3 group to the phenyl ring of styrene in toluene solutions.

In addition to rotations about X_4/X_5, other modes that could contribute to the mobility of nitroxide side chains at site 72 include torsional oscillations about bonds 1, 2, and 3 within the nitroxide side chain, torsional oscillations within the backbone and rigid body rocking motions of the helix. Collectively, the evidence discussed above clearly implicates torsional oscillations about bonds 4 and 5 as key contributors to the mobility of the side chains. The relatively high activation free energy reported for disulfide bond isomerizations in small molecules in solution [$\Delta G^o_{activation} = 6.6-9.0$ kcal/mol (*11*)] give rates in the range 9×10^5 to 7×10^7 s^{-1}, as compared to the rates of $\approx 5 \times 10^8$ s^{-1} deduced from spectral simulations. For the R1 series (or the R5 series) on a helix, the interaction of the S_δ with the backbone (*10*) would likely reduce isomerization rates even further. Nevertheless, small amplitude torsional oscillations of X_3, and X_1 and X_2 as well, probably contribute to the nitroxide motion to some extent. At site 72, motions originating in the backbone are assumed to be relatively small, for the reasons discussed in the introduction. Backbone contributions to the motion of R1(a) at 131 and other sites will be discussed below.

Motion of the R5(x) Side Chain and the Absence of a 4-Substituent Effect. (a) The X_4/X_5 Model Accounts for the Effect of Ring Geometry on the EPR Spectra. A further test of the X_4/X_5 model for internal motion is afforded by changing the ring geometry through saturation of the double bond. In the saturated analogue R5(a), there are two enantiomers (R and S) due to the chiral 4-carbon of the nitroxide ring, as shown in Figure 12, panels B and C. In the present experiments, a racemic mixture of the spin labeling reagent V was employed. The racemic mixture has been resolved, and preliminary studies show that both enantiomers give nearly identical spectra at site 72 (Kálai, Columbus, Hubbell and Hideg, unpublished observations). Experimentally, the EPR spectrum of 72R5(a) reveals a striking increase in averaging of the nitroxide magnetic anisotropies relative to that for 72R1(a) at the same temperature (Figure 7). Inspection of a minimized structure of the R5 side chain reveals that the important difference between R1(a) and either enantiomer of R5(a) is the orientation of the bond 4 and 5 axes with respect to the nitroxide p orbital axis (z_M) and the steric constraints on rotations about these axes (Figure 12). For purposes of an approximate discussion, the rotation axes of X_4 and X_5 in both enantiomers (Figure 12, panels B and C) are roughly perpendicular ($\approx$110°) and parallel ($\approx$20°) to the nitroxide p orbital, respectively. This situation is essentially opposite to that in R1(a), and corresponds to the z_R axis of the diffusion tensor being closer to perpendicular rather than parallel to the nitroxide p orbital. Indeed, the spectrum of 72R5(a) can be simulated with the same parameter set used for 72R1(a), except that the diffusion angle β_D is increased from 36° to any value in the range $80° \leq \beta_D \leq 120°$. For the orientation of the z_R axis defined by β_D in this range (essentially perpendicular to the nitrogen 2p orbital), the major anisotropies ($A_{zz}-A_{yy}$, $g_{xx}-g_{zz}$) are effectively averaged by rotations about bond 4, giving rise to the narrow resonance lines.

(b) The X_4/X_5 model offers an explanation for the absence of the 4-substituent effect in the R5(x) Series. The effect of 4-substituents in the R5(x) series is particularly revealing. In the saturated R5(x) series with 4-substituents, each member has four possible isomers. There are two enantiomeric pairs: 3R/4S, 3S/4R and 3R/4R, 3S/4S, where the numerals refer to the carbon in the nitroxide ring. In the later pair, the 3- and 4-substituents are in a cis configuration and are excluded on the basis of the synthetic method used to prepare the corresponding reagents, which gives exclusively the trans configuration (*22*). Thus, the racemic mixture employed contains and equal mixture of 3R/4S and 3S/4R. These enantiomers can be visualized by adding a trans 4-substituent to the enantiomers of Figure 12, panels B and C.

The effect of 4-substituents in the R5(x) series of side chain motion is fundamentally different than that observed for the R1(x) series. For example, 72R1(b) with a 4-methyl group is rather strongly immobilized relative to 72R1(a), while 72R5(b) is only slightly different in mobility from 72R5(a). Again, this difference is expected from the X_4/X_5 internal rotation model. As discussed above, the 4-substituent hinders rotation about bond 5 in the series R1(x), and thereby defines the ordering potential. In the saturated R5(x) series, the substituent in either enantiomer does *not* bump into either sulfur atom under rotation about bond 4 or 5, but simply orbits the sulfur as illustrated for one isomer in Figure 13, panel B. However, larger substituents e−g in the 72R5(x) series do lead to an immobilization of the side chain greater than expected from the model discussed above, although the immobilization is still generally less than in the 72R1(x) counterpart (Figure 7). The immobilization due to these bulky substituents could arise from interactions with nearest neighbor side chains, with main chain atoms, or possibly interactions with the disulfide or tethering regions of the nitroxide side chain.

Site-Specific Side Chain Motion: Contributions from Backbone Dynamics. The internal anisotropic motion of 131R1(a) can be accurately simulated using the same parameters as for 72R1(a), but with a smaller order parameter corresponding to a slight increase in the mean angular

displacement of the z_R diffusion axis ($\Delta(\langle\theta\rangle) \approx 5°$) and hence a higher amplitude of motion.

The origin of the mobility difference between 72R1(a) and 131R1(a) at physiological temperature is of particular interest. The mobility difference could arise from different rotameric states of the side chain stabilized by different interactions with the immediate environment. However, at physiologic temperatures, there is no evidence for such interactions at either site. Indeed, previously published data showed that mutation of nearest neighbors around 72R1(a) and 131R1(a) to create the same immediate side chain environment at these solvent-exposed sites does not cause the mobility to become similar to each other (*4*). A more attractive proposal is that the mobility difference reflects dynamic differences in the helical backbone itself, arising from structural and environmental differences between the two helices. For example, the 131 helix consists of only two and a half-turns, hardly long enough for end effects to decay at the central 131 site (*43*, *44*). On the other hand, site 72 is located in the center of a long 5-turn helix. The 72 helix has a stabilizing threonine N-cap, while the 131 helix has two positively charged residues in the N-capping box, which are poor helix caps (*45*). Perhaps most importantly, the segment of the helix that contains site 72 is located near the tightly packed hydrophobic core of a helix bundle. These features, in addition to experimental data such as higher crystallographic Debye−Waller factors (*12*) and H exchange rates (*13*) at 131 as compared to 72, lead to the intuitively reasonable view that the higher mobility of 131R1(a) may have its origin in larger amplitude backbone fluctuations near 131 due to an intrinsically lower thermodynamic stability of the secondary structure.

For example, the higher mobility of 131R1(a) relative to 72R1(a) could be due to backbone fluctuations of the type detected in NMR through the N-H bond order. In fact a maximum difference in order parameter corresponding to an angular amplitude difference of ≈5° was detected between two helices (α_D and α_E) in ribonuclease H (*46*). This amplitude difference is very similar to that observed between 131R1(a) and 72R1(a) ($\Delta(\langle\theta\rangle) \approx 5°$), but it is not possible to decide if the backbone modes characterized by NMR could account for the EPR data without having more information on the nature of the modes and the orientation of the nitroxide ring relative to the helix axis. It is also possible that the helix dynamic mode observed in the EPR spectra is rigid-body rocking (*47*) or a local unfolding (i.e., "fraying" of the helix) (*43*, *44*). However, it is not likely that the latter is the origin of the difference between 131 and 72 considering the high activation energy and lower frequencies involved in hydrogen bond breaking (i.e., partial unfolding of helix 131) (*48*).

Figure 14 compares the EPR spectra of R1(a) on solvent-exposed helical sites of colicin E1 (*7*), annexin XII (*8*), and sites 72 and 131 of T4 lysozyme. Remarkably, each site displays the characteristic anisotropic line shape, which can be simulated by the same model for anisotropic motion and rationalized by the X_4/X_5 model. However, each site differs quantitatively in the order parameter and perhaps rates, with site 72 being the most ordered based on the overall breadth of the spectrum. The difference in mobility between these sites is not due to differences in overall correlation times of the proteins, because the spectra were recorded in high viscosity where the correlation time is in the slow-motion limit for X-band EPR. Rather, the differences likely reflect different amplitudes and possibly rates of backbone motions. The structural origins of these differences will be discussed elsewhere.

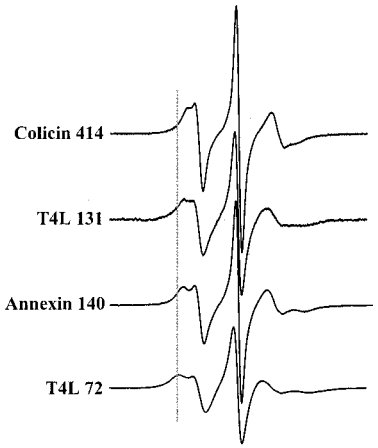

FIGURE 14: Experimental EPR spectra of R1(a) on solvent-exposed helical sites of colicin E1 (414), T4L (131), annexin (140), T4L (72) in decreasing order of mobility from top to bottom. The gray vertical line is drawn as a reference to guide the eye for comparison.

Interaction of the Nitroxide Side Chain with the Environment: A Probe of Tertiary Structure. The structure of 119R1(a) at 1.4 Å resolution was recently published and revealed the existence of two equally populated rotameric states of R1(a) corresponding to two sets of values for X_1 and X_2. One rotameric state (X_1, X_2 = 175, 54) is apparently stabilized by interaction of the disulfide with an *i+4* glutamine. The environment of the nitroxide in the rotamers is different, resulting in a two-component EPR spectrum at room temperature (Figure 11). Mutation of the *i+4* glutamine to alanine results in a redistribution of the spectral populations (*5*). Thus, 119R1(a) is a relatively well understood model system for exploring the nature of the R1(a) nitroxide-environment interaction. In the present study, this site is used for comparative purposes and to illustrate the use of temperature in revealing or abolishing interactions.

The temperature dependence of 119R1(a) clearly reveals the two-state nature of the spectrum, particularly at temperatures below 24 °C (Figure 11), where one component is essentially immobilized, clearly distinguishing it from a second spectral feature that has features characteristic of an anisotropic motion. At higher temperature, above about 32 °C, the more immobilized component disappears, leaving an apparently single population of mobile spins.

In a similar fashion, the spectrum of R1(a) at site 131 (but not 72) clearly reveals a second component at reduced temperatures but not at room temperature (Figure 9). Presumably, the two-component nature of the spectrum of 131R1(a) at low temperature arises from a weak interaction of the ring with the protein environment as in 119R1(a), although not necessarily corresponding to two rotameric states.

In 119R1(a) and 131R1(a), the two populations are roughly equal around $T_{e,119} \approx 297$ K (24 °C) and $T_{e,131} \approx 273$ K (0 °C), respectively. At these temperatures, the equilibrium constant ≈ 1 and $\Delta H° = T\Delta S°$, where the thermodynamic parameters refer to differences between the interacting (immobilized) and noninteracting states. Thus, $T_{e,119}/T_{e,131} = [\Delta H°/\Delta S°]_{119}/[\Delta H°/\Delta S°]_{119} \approx 1.1$. With the reasonable

assumption that the entropy difference between the mobile and immobile states for the same side chain are similar in the two cases, this ratio is approximately the ratio of interaction energies. Thus, about a 10% difference in the enthalpy of interaction can account for the difference in observing or not observing the interaction in the spectrum at a particular temperature.

As an order of magnitude estimate, the entropy change for R1(a) may be computed according to Kauzmann (*49*), assuming that the immobilized state has a single configuration and the mobile state has two degrees of freedom (bonds 4 and 5) with two configurations for each. Thus, $\Delta S^\circ \approx R\ln 2^2$. Assuming a similar entropy loss for a native side chain in the protein due to the immobilizing interaction with the spin label, this gives $\Delta S^\circ_{conf} \approx -5.4$ cal/K·mol. For 119R1(a), the corresponding $\Delta H^\circ = T\Delta S^\circ \approx -1.6$ kcal/mol (at 297 K). Although highly approximate, these calculations emphasize the sensitivity of the EPR spectra to weak interactions and to small differences in interaction energy. Clearly, temperature is an important variable that can be used to titrate weak interactions with the environment.

The weak interaction observed in 131R1(a) at lower temperatures is also apparent at physiological temperatures for R1(x) side chains bearing 4-substituents, as evidenced by the unusually broad lines that cannot be simulated by a single dynamic population of side chains (Figure 10). It is likely that the substituents establish tertiary interactions with nearby structures (or within the same helix), and the spectrum represents a superposition of mobility states, which may be in exchange on the EPR time scale. Even at site 72, the large phenyl and phthalidimido substituents of R1(f) and R1(g) probably establish interactions with the environment and give rise to EPR spectra in the slow motion regime (Figure 6).

For the R5(x) series, the effect of nitroxide interaction with the environment may also be reflected in the EPR spectra. For example, although the smaller methyl and carboxamido substituents have little effect on mobility of R5(x) at 72, the larger substituents are anomalously immobile (Figure 7), possibly due to tertiary contact interactions, interactions with the local backbone, or interactions within the side chain itself.

Tertiary interactions of the nitroxide side chain as reflected in the mobility and the EPR spectra can be a powerful tool for the investigation of conformational changes in proteins (*3*), because of the modulation of such interactions produced by changes in the tertiary fold. For this purpose, the detection of interactions is desired, and the use of the R1(x) and R5(x) series with 4-substituents, or the use of slightly reduced temperature, may prove to be an important strategy in tertiary structure mapping by SDSL. On the other hand, for mapping secondary structure such interactions may be a hindrance (*5*), and the use of R1(a) at a slightly elevated temperature is advocated based on the studies presented here.

General Summary, and Implications of the Results for New Applications of the Side Chains. A primary result of the work presented here is a description of the salient features of the internal dynamic mode of the R1(a) side chain at solvent-exposed helical surface sites. At such sites, in the absence of interactions with the environment, the internal dynamic mode of R1(a) may be treated as site-independent. Site-specific differences in side chain motion are tentatively assigned to dynamic contributions from backbone modes, either torsional oscillations about main chain bonds, or rigid-body helix motions.

The 4-methyl substituent in R1(b) attenuates internal motion within the side chain by hindering internal bond rotations. Therefore, the contribution to the overall motion from backbone modes is enhanced. This being the case, the R1(b) derivative may prove to be a useful probe for backbone dynamics, although the motion may have to be analyzed by means other than CW X-band EPR, because of the low spectral sensitivity to small differences in motion near the slow motion limit.

The internal mode of motion of R1(a) can be additionally modulated by tertiary interaction of the nitroxide with the protein environment. The interaction can be effectively titrated with temperature and enhanced by the addition of a sufficiently bulky 4-substituent. For the purposes of detecting conformational changes through modulation of tertiary interactions, the R1(x) series of spin labels offer a novel approach. For large 4-substituents, local interactions strongly immobilize the side chain. Thus, the R1(g) reagent may find use as a monitor for the rotational motion of the whole protein. This capability is particularly useful in monitoring protein−protein interactions through changes in the rotational correlation time of the interacting species.

In the R5(x) series, unlike the case for the R1(x) series, small 4-substituents do not significantly reduce the amplitude of internal motions within the side chain. Thus, the R5(x) series has an important practical application based on a nitroxide side chain that mimics the properties of the native side chain. For example, a positively charged 4-substitutent may mimic the electrostatic properties of a lysine or arginine residue. Because the mobility of the side chain is not strongly affected by the presence of the substituent, modulation of the mobility may be used to detect salt-bridge formation. Other side chain mimics would include those with anionic carboxylate substituents and hydrogen bonding capabilities [such as R1(h)].

ACKNOWLEDGMENT

We thank Dr. Thomas Risse and Dr. Christian Altenbach for scientific discussion; Dr. Thomas Risse for helpful comments on the manuscript; Dr. David Budil for the MOMD simulation program and guidance in its application; and Dr. Ralf Langen for contributing some of the temperature data for 119R1.

REFERENCES

1. Hubbell, W. L., McHaourab, H. S., Altenbach, C., and Lietzow, M. A. (1996) *Structure 4*, 779−83.
2. Hubbell, W. L., Gross, A., Langen, R., and Lietzow, M. A. (1998) *Curr. Opin. Struct. Biol. 8*, 649−56.
3. Hubbell, W. L., Cafiso D. S., and Altenbach, C. (2000) *Nat. Struct. Biol. 7*, 735−739.
4. Mchaourab, H. S., Lietzow, M. A., Hideg, K., and Hubbell, W. L. (1996) *Biochemistry 35*, 7692−704.
5. Mchaourab, H. S., Kálai, T., Hideg, K., and Hubbell, W. L. (1999) *Biochemistry 38*, 2947−55.
6. Salwinski, L., and Hubbell, W. L. (1999) *Protein Sci. 8*, 562−572.
7. Langen, R., Isas, J. M., Hubbell, W. L., and Haigler, H. T. (1998) *Proc. Natl. Acad. Sci. U.S.A. 95*, 14060−5.
8. Oh, K. J., Zhan, H., Cui, C., Hideg, K., Collier, R. J., and Hubbell, W. L. (1996) *Science 273*, 810−2.

9. Langen, R., Oh, K. J., Cascio, D., and Hubbell, W. L. (2000) *Biochemistry 39*, 8396−405.
10. Fraser, R. R., Bousard, G., Saunders, J. K., Lambert, J. B., and Mixan, C. E. (1971) *J. Am. Chem. Soc. 93*, 3822.
11. Weaver, L. H., and Matthews, B W. (1987) *J. Mol. Biol. 193*, 189−199.
12. Anderson, D. E., Lu, J., McIntosh, L., and Dahlquist, F. W. (1993) in *NMR of Proteins* (Clore, G. M., Gronenborn, A. M., Ed.) pp 258−304, CRC Press, Boca Raton, FL.
13. Berliner, L. G., Grunwald, J., Hankovszky, H.O., and Hideg, K. (1982) *Anal. Biochem. 119*, 450−455.
14. Sár, P. C., Jekö, J., and Hideg, K. (1998) *Synthesis* 1497−1500.
15. Kálai, T. B., M., Jekö, J., and Hideg, K. (1998) *Synthesis* 1476−1482.
16. Kálai, T., Balog, M., Jekö, J., and Hideg, K. (1999) *Synthesis* 973−980.
17. Hankovszky, H. O., Hideg, K., Sár, P. C., Lovas, M. J., and Jerkovich, G. (1990) *Synthesis* 59−62.
18. Kálai, T., Rozsnyai, B., Jerkovich, G., and Hideg, K. (1994) *Synthesis*, 1079−1082.
19. Kálai, T., Bárácz, M. N., Jerkovich, G., Hankovszky, H. O., and Hideg, K. (1995) *Synthesis*, 1278−1282.
20. Rozantsev, E. G. (1970) *Free Nitroxyl Radicals*, Plenum Press, New York.
21. Hideg, K., Hankovszky, H. O., Halász, H. A., and Sohár, P. J. (1988) *J. Chem. Soc., Perkin I.*, 2905−2911.
22. Hideg, K., Hankovszky, H. O., Lex, L., and Kulcsár, G. (1980)-*Synthesis*, 911−914.
23. Sauer, U. H., San, D. P., and Matthews, B. W. (1992) *J. Biol. Chem. 267*, 2393−2399.
24. Ho, S. N., Hunt, H. D., Horton, R. M., Pullen, J. K., and Pease, L. R. (1989) *Gene 77*, 51−59.
25. Hubbell, W. H., Froncisz, W., and Hyde, J. S. (1987) *Rev. Sci. Instrum. 58*, 1879−1886.
26. Timofeev, V. P., and Tsetlin, V. I. (1983) *Biophys. Struct. Mech. 10*, 93−108.
27. Langen, R., Cai, K., Altenbach, C., Khorana, H. G., and Hubbell, W. L. (1999) *Biochemistry 38*, 7918−24.
28. Schneider, D. J., and Freed, J. H. (1989) in *Biological Magnetic Resonance* (Berliner, L. J., Reuben, J., Ed.) pp 1−76, Plenum Publishing Corporation, New York, NY.
29. Budil, D. E., Lee, S., Saxena S., and Freed. J. H. (1996) *J. Magn. Reson., Series A 120*, 155−189.
30. Barnes, J. P., Liang, Z., Mchaourab, H. S., Freed, J. H., and Hubbell, W. L. (1999) *Biophys. J. 76*, 3298−3306.
31. Hubbell, W. L., and McConnell, H. M. (1971) *J. Am. Chem. Soc. 93*, 314−326.
32. Griffith, O. H., and Jost, P. C. (1976) in *Spin Labeling Theory and Applications* (Berliner, L. J., Ed.) pp 454−523, Academic Press, New York.
33. Mason, R. P., Polnaszek, C. F., and Freed, J. H. (1974) *J. Phys. Chem. 78*, 1324−1329.
34. Mason, R. P., and Freed, J. H. (1974) *J. Phys. Chem. 78*, 1321−1323.
35. Gaffney, B. J., and McConnell, H. M. (1974) *J. Magn. Reson. 16*, 1−28.
36. Gross, A., Columbus, L., Hideg, K., Altenbach, C., and Hubbell, W. L. (1999) *Biochemistry 38*, 10324−35.
37. Freed, J. H. (1976) in *Spin Labeling Theory and Applications* (Berliner, L. J., Ed.) pp 53−132, Academic Press, New York.
38. Powles, J. G., and Figgins, R. (1966) *Mol. Phys. 10*, 156.
39. Sober, H. (1970) *CRC Handbook of Biochemistry Selected Data for Molecular Biology*, 2nd ed., The Chemical Rubber Co., Cleveland.
40. Bullock, A. T., and Cameron, G. G. (1976) in *Structural Studies of Macromolecular Spectroscopic Methods* (Ivin, K. J., Ed.) pp 273−315, Wiley, Chichester, England.
41. Pilar, J., Kalal, J., and Freed, J. H. (1979) *J. Phys. Chem. 83*, 1907−14.
42. Mikhailov, D., Daragan, V. A., and Mayo, K. H. (1995) *J. Biomol. NMR 5*, 397−410.
43. Lifson, S., and Roig, A. (1961) *J. Chem. Phys. 34*, 1963−1974.
44. Zimm, B. H., and Bragg, J. K. (1959) *J. Chem. Phys. 31*, 526−535.
45. Doig, A. J., and Baldwin, R. L. (1995) *Protein Sci. 4*, 1325−1336.
46. Mandel, A. M., Akke, M., and Palmer, A. G. (1996) *Biochemistry 35*, 16009−16023.
47. Fischer, M. W. F., Zeng, L., Pang, Y., Hu, W., Majumdar, A., and Zuiderweg, E. R. P. (1997) *J. Am. Chem. Soc. 119*, 12629−12642.
48. Woodward, C., Simon, I., and Tüchsen, E. (1982) *Mol. Cell. Biochem. 48*, 135−160.
49. Kauzmann, W. (1954) in *A Symposium on the Mechanism of Enzyme Action* (McElroy, W. D., Glass, B., Ed.) pp 70−110, Johns Hopkins Press, Baltimore.

BI002645H